Termination of a continent-margin upwelling system at the Permian-Triassic boundary (Opal Creek, Alberta, Canada)

Shane D. Schoepfer[1]*

Charles M. Henderson[2]

Geoffrey H. Garrison[1]

Julien Foriel[3]

Peter D. Ward[1]

David Selby[4]

James C. Hower[5]

Thomas J. Algeo[6]

Yanan Shen[7]

[1] Department of Earth and Space Sciences, University of Washington, Seattle, WA 98195, U.S.A.

[2] Department of Geoscience, University of Calgary, Calgary, AB, Canada

[3] Department of Earth and Planetary Science, Washington University, St. Louis, MO 63130, U.S.A.

[4] Department of Earth Sciences, Durham University, Durham, DH1 3LE, U.K.

[5] Center for Applied Energy Research and Department of Earth & Environmental Sciences, University of Kentucky, Lexington, KY 40506, U.S.A.

[6] Department of Geology, University of Cincinnati, Cincinnati, OH 45221 U.S.A.

[7]Chinese Academy of Sciences Key Laboratory of Crust-Mantle Materials and Environments, School of Earth and Space Sciences, University of Science and Technology of China, Hefei 230026, China

ABSTRACT

Models of mass extinctions caused by greenhouse warming depend on the ability of warming to affect the oxygenation of the ocean, either through slowing circulation or changes in biological productivity and the organic carbon budget. Opal Creek, Alberta, Canada is a biostratigraphically continuous Permian-Triassic Boundary (PTB) section deposited in deep water on an outer shelf setting in the vast and understudied Panthalassic Ocean, along the western margin of Pangaea. The end-Permian extinction is here represented as the disappearance of the previously dominant benthic fauna (siliceous sponges). On the basis of nitrogen and reduced sulfur isotopes as well as productivity-sensitive trace elements, the Middle Permian at Opal Creek is interpreted as a highly productive coastal upwelling zone where vigorous denitrification and sulfate reduction occurred in a mid-water oxygen minimum. Similar conditions appear to have continued into the latest Permian until the onset of a euxinic episode represented by a discrete pyrite bed and several trace element indicators of high productivity. This euxinic pulse is followed by the extinction of benthic fauna and a shift in nitrogen and sulfur isotopes to more normal marine values, suggesting the cessation of coastal upwelling and the consequent weakening of the mid-water oxygen minimum. The Lower Triassic appears to be a dysoxic, relatively unproductive environment with a bottom water oxygen minimum. Rhenium-Osmium isotope systematics show a minimum of radiogenic Os near the main extinction event, which may be due to volcanic input, and increasingly radiogenic values approaching the PTB, possibly due to increased continental erosion. The Opal Creek system demonstrates

that, while the biogeochemical crisis in the latest Permian was capable of impacting the coastal upwelling modality of ocean circulation, a transient increase in productivity likely drove the system toward euxinia and, ultimately, extinction.

Key words: Permian; extinction; Panthalassic; marine productivity; upwelling; anoxia

1. Introduction

The latest Permian mass extinction (LPME), at ~252 Ma, was the greatest biodiversity crisis of the Phanerozoic (Erwin et al., 2002), fundamentally and permanently altering terrestrial and marine ecosystems (Benton et al., 2004; Bottjer et al., 2008). The trigger for this crisis is thought to have been eruption of the Siberian Traps flood basalts (Wignall, 2007; Reichow et al., 2009), which led to strong global warming as a consequence of emissions of CO_2 and possibly methane (Payne and Kump, 2007; Retallack and Jahren, 2008). Climatic warming or related effects led to perturbations of terrestrial environments, including changes in weathering patterns, aridification, vegetation loss, and fluvial drainage alteration (Retallack, 1999; Looy et al., 1999, 2001; Ward et al., 2000). In the marine realm, warming is thought to have been an important factor in reduced deepwater ventilation, a buildup of hydrogen sulfide, hypercapnia, seawater acidification, and depletion of certain nutrients such as nitrate (Knoll et al., 1996; Kump et al., 2005; Fraiser and Bottjer, 2007; Luo et al., 2011). The development of global greenhouse conditions at this time is paleontologically evident in the appearance of warm-climate floras at polar latitudes (Taylor et al., 2000), the demise of high-latitude, cool-water siliceous sponge communities (Henderson, 1997; Beauchamp and Baud, 2002), and a breakdown of temperature-based conodont provincialism (Mei and Henderson, 2001).

Direct evaluation of changes in Permian-Triassic ocean circulation patterns has proven difficult, owing to the relative paucity of preserved PTB sections from the Panthalassic Ocean, which covered some 70% of the globe at the time of the extinction (Fig. 1) and hence is central to investigations of global change related to the LPME. . Extant Panthalassic sections are limited to a few areas and depositional facies, including deep-sea cherts (Isozaki, 1994, 1997; Algeo et al., 2010, 2011b; Sano et al., 2010) and shallow atoll carbonates from Japan (Musashi et al., 2001), volcanic-arc slope sediments in New Zealand (Krull et al., 2000), and a series of deep-shelf or upper slope siliciclastic successions in western North America (Beauchamp and Baud, 2002; Wignall and Newton, 2003; Hays et al., 2007). Anoxic facies have been documented at widespread Permian-Triassic boundary (PTB) sections, leading some workers to infer that such redox changes were global in extent, and due to strongly reduced overturning circulation ("ocean stagnation") (Isozaki, 1994, 1997; Wignall and Twitchett, 1996, 2002). Paleoceanographic modeling studies have demonstrated that, while strong climatic warming could slow the meridional overturning circulation significantly, it would generally not be sufficient to generate the persistent, highly reducing conditions necessary to drive surface euxinia without a substantial increase in nutrient availability (Hotinski et al., 2001; Meyer et al. 2008). Modeling of paleoceanographic conditions at the PTB generally supports the hypothesis that overturning circulation persists despite extreme greenhouse conditions (Kiehl and Shields, 2005; Winguth and Maier-Reimer, 2005).

Recently, attention has focused on the role of increased nutrient inventories in ocean-surface waters, and consequent increases in marine primary productivity, in driving PTB oceans toward anoxia (Algeo et al., 2011a). This hypothesis has received support from studies demonstrating a substantial expansion of the mid-ocean oxygen-minimum zone in

periequatorial regions (Algeo et al., 2010, 2011b) as well as a steepening of shallow-to-deep carbon isotopic gradients in epicratonic seas (Meyer et al., 2011; Song et al., in review).

[Insert Figure 1]

In this study, we examine changes along the eastern margin of the subtropical Panthalassic Ocean between the Early Permian and Early Triassic. Our primary goal is to test models of anoxia-development in the Panthalassic ocean by collecting field geochemical evidence for changes in circulation and organic productivity rates during the PTB transition interval. The site for this study is the Opal Creek section in southwestern Alberta, which represents an outer-shelf or upper slope setting on the western margin of the North American plate at a paleolatitude of ~30°N (Henderson, 1989, Richards, 1989). As shown by both field data and paleoceanographic modelling, this region was characterized by strong upwelling during much of the Permian (Ziegler et al., 1998, Beauchamp and Baud, 2002, Winguth and Maier-Reimer, 2005), a mode of circulation potentially sensitive to global climate changes. A shift in ocean circulation patterns is suggested by major changes in boreal marine biotas during the Late Permian (Henderson and Baud, 1997; Beauchamp and Baud, 2002; Gates et al., 2004; Beauchamp et al., 2009), culminating in a regional extinction of sponges in the late Changhsingian (Algeo et al., 2012), as well as a shift from the enriched nitrogen isotope values characteristic of coastal upwelling zones to values characteristic of more nitrogen-limited environments (Schoepfer et al. 2012). Here, we present sulfur isotope and trace-element concentration data in order to (1) document changes in redox conditions, productivity, and euxinia within the upwelling system of the eastern subtropical Panthalassic Ocean during Early Permian to Early Triassic, and (2) evaluate the relationship of changes in this region during the PTB transition to broader changes in the global environment based on detailed biostratigraphic correlations (Henderson et al., 1994; Henderson, 1997).

2. Geologic setting and biostratigraphy

The Opal Creek section is located in the Kananaskis Valley, in the foothills of the Canadian Rockies west of Calgary (Fig. 1). It comprises ~25 meters of Lower Permian through Lower Triassic strata assigned to the Johnston Canyon, Ranger Canyon, and Sulphur Mountain formations. Beds dip nearly vertically, with cherts and silicified siltstones forming prominent cliffs while more fissile siltstones are exposed in hill slopes (Fig. 2). The thermal maturity of the section is moderate, as shown by a conodont color alteration index (CAI) of ~2.5 (Schoepfer et al., 2012), equivalent to a maximum burial temperature of ~150°C (Tissot and Welte, 1984; Hunt, 1996). Similar maturity levels have been inferred for other PTB sections in the Canadian Western Sedimentary Basin on the basis of vitrinite reflectance (Radke et al., 1982), CAI (Utting et al., 2005), and biomarker studies (Hays et al., 2007).

[Insert Figure 2]

The Early Permian is represented by the Johnson Canyon Formation (Fig. 3), which is composed of silty dolostone containing abundant nodular phosphate layers. This unit exhibits lithologic cyclicity, likely as a consequence of glacio-eustatic fluctuations during the Early Permian, when ice is believed to have existed at the poles (Haq and Schutter, 2008).

The Middle Permian is represented by the Ranger Canyon Formation (RCF, Figs. 3-4), which (together with its stratigraphic equivalent, the Fantasque Formation) extends from southeastern British Columbia northward to the southern Mackenzie Fold Belt in the Yukon (Henderson, 1989). The Ranger Canyon, which is just 2.35 m thick at Opal Creek, consists of completely bioturbated, recrystallized spiculitic chert to cherty immature siltstone containing microcrystalline carbonate cements and some reworked chert and carbonate grains. The predominance of sponge spicules, abundance of phosphatic material

including abundant conodonts, and the absence of shallow-water sedimentary structures (Henderson, 1997) suggest an outer shelf or slope environment at a few hundred meters water depth, below storm wave base and probably oligophotic. The most common fossils are large monaxon siliceous sponges spicules (up to 6 cm long), possibly of the class Demospongea. Also abundant are conodonts of the genus *Mesogondolella,* which in the Middle and Late Permian are indicative of cool-water environments, as inferred from their boreal provincialism (Mei and Henderson 2001). The main species are *M. bitteri* and, toward the top of the formation, *M. rosenkrantzi*, indicating a Capitanian age or, where *M. rosenkrantzi* is found without *M. bitteri*, an early Wuchiapingian age (Henderson and Mei, 2007).

The upper contact of the RCF is defined by a major regional unconformity, coinciding with the Guadalupian-Lopingian lowstand (Haq and Schutter, 2008). On the basis of the conodont biostratigraphy, the duration of this unconformity has been estimated at 5-7 million years. The Late Permian and Early Triassic are represented by the Phroso Siltstone Member of the Sulphur Mountain Formation (SMF; Figs. 3-4), which is equivalent to the Grayling Formation in northeastern British Columbia (Wignall and Newton, 2003). The basal ~10 m of this unit represent a trangressive systems tract (TST) characterized by an upward fining succession. Sediments consists of angular, immature silt to fine sand and contains dolomite rhombs as well as reworked chert, micas, and microcrystalline carbonate. Pyrite is also present, concentrated around organic fragments and, especially, in a cm-thick bed that is ~10.5 cm above the basal unconformity. The lowermost beds of this unit are bioturbated and contain abundant siliceous monaxon sponge spicules up to 2 cm in length, but these features disappear abruptly ~40 cm above the basal unconformity. At the same level, the conodont fauna dominated by *Mesogondolella* is abruptly replaced by a new fauna dominated by the genus *Clarkina,* a transition that probably marks the latest Permian mass

extinction event (see below). Above this level, the SMF is composed of black to dark grey, pyritic, thin-bedded shale and siltstone. Benthic biota and bioturbation are lost, suggesting suboxic to anoxic bottom waters during deposition (Fig. 2) (Gibson, 1969, 1974; Gibson and Barclay, 1989; Henderson, 1997).

Four conodont biozones are present in the Sulphur Mountain Formation (Figs. 3-4), in ascending order:

1) *Mesogondolella sheni* Zone—Specimens of *M. sheni* from the basal TST of this formation indicate a Changhsingian age, but the exact relationship between these specimens and the type material from Selong, Tibet (Mei, 1996; Shen et al., 2006) remains uncertain. Specimens of *M. rosenkrantzi* and *M. bitteri* are considered to have been reworked from the underlying Ranger Canyon Formation during the transgression. The extent of reworking is difficult to address since all specimens are fragmented in these deformed shale units. At Ursula Creek in northeastern British Columbia, the uppermost Fantasque Formation contains both *M. sheni* and *M. rosenkrantzi*, indicating a Changhsingian age (Henderson, 1997; Wignall and Newton, 2003). We suggest a Late Changhsingian age for this assemblage at Opal Creek given that indisputably latest Changhsingian species are recovered only 40 cm higher in the section.

2) *Clarkina hauschkei–Clarkina meishanensis* Zone—This zone is defined by the association of *C. hauschkei*, *C. meishanensis*, *C. cf. changxingensis*, and *C. cf. zhejiangensis*. A comparable assemblage was recovered from the basal Blind Fiord Formation in the Canadian Arctic (Algeo et al., 2012). *C. hauschkei* is similar to specimens described as *C. hauschkei borealis* by Kozur (2005) from a zone immediately below the end-Permian microbialite facies at Abadeh, Iran. *C. meishanensis sensu stricto* is restricted to Beds 25 to 28 at Meishan (Jiang et al., 2007), but a similar species *C. zhangi* originally described as a

subspecies of *C. meishanensis* (Mei et al., 1998) ranges from Bed 23 to 24e at Meishan. These two species may be synonymous and therefore range from Late Permian (Bed 23) to Lower Triassic (Bed 28). Kozur (2005) indicated that *C. meishanensis* migrated into Iran during the late Changhsingian, correlative with the Bed 23-24e interval at Meishan. At Opal Creek, the base of this zone is marked by a sharp reduction in *Mesogondolella* (which survives to the PTB) and the appearance of the genus *Clarkina*. The latter genus is typical of the equatorial warm-water province during the Late Permian (Mei and Henderson, 2001), and its appearance in the Canadian Western Sedimentary Basin is thus indicative of a breakdown of a temperature barrier to migration (Henderson and Mei, 2007). The faunal turnover at Opal Creek is either equivalent in age to, or slightly precedes that of, the main extinction horizon (Bed 25) at Meishan, China (Jin et al., 2000).

3) *Hindeodus parvus–Clarkina taylorae* Zone—*H. parvus* is the key marker for the base of the Triassic at the GSSP in Meishan, China (Yin et al., 1996, 2001); its occurrence elsewhere does not define the PTB, but according to chronostratigraphic principles indicates only proximity to it within the *H. parvus* Zone (Henderson, 2006). At Meishan and elsewhere, the lowermost Triassic is typically characterized by a short-term acme of *Hindeodus* (Chen et al., 2009; Jiang et al., 2007; Zhang et al., 2007). Although this genus is rare at Opal Creek, some small, poorly preserved specimens were found in the lower ~6 m of the SMF. The local first occurrence of *H. parvus* is ~1.5 m above the base of the SMF, where it is found in association with *C. taylorae.* The latter taxon has not been recovered with certainty below the PTB (Orchard et al., 1994), so the co-occurrence of these two species is probably a good marker for the stratigraphic position of the PTB at Opal Creek.

4) *Clarkina taylorae–Clarkina cf. carinata* Zone—*C. carinata* (= *Neogondolella* of some authors) is the most commonly identified Lower Triassic conodont species (Clark,

1959; Orchard and Krystyn, 1998; Sweet, 1970). The co-occurrence of *C. taylorae* and *C. cf. carinata* indicates a Griesbachian (Lower Induan) age.

3. Materials and methods

3.1. Field protocol

A total of 55 samples were collected over a 30-m-thick stratigraphic interval ranging from the Lower Permian Johnston Canyon Formation through the Lower Triassic Sulphur Mountain Formation for analysis of S isotopic compositions, S speciation, and trace-metal concentrations, with collection concentrated in the basal Sulphur Mountain Formation, around the extinction and boundary. An additional 14 samples were collected over a 1.4-m-thick stratigraphic interval at the base of the Sulphur Mountain Formation for analysis of Re-Os abundances and Os isotopic compositions. Samples were collected at 10 cm spacing from 20 cm above the Ranger Canyon/Sulphur Mountain unconformity to a level 1.6 m above the unconformity.

A separate set of 99 samples was collected at 40 cm intervals from the basal 44 m of the SMF, and processed at the University of Cincinnati. Carbon and sulfur elemental concentrations were determined using an Eltra 2000 C-S analyzer, and results calibrated using USGS and internal laboratory standards. Analytical precision was better than ±2.5% for carbon and ±5% for sulfur. An aliquot of each sample was digested in HCl at 50ºC for 12 hours, washed and filtered, and reanalyzed for C and S in order to determine concentrations of total organic carbon (TOC) and non-acid volatile sulfur (NAVS). These data are presented in Figure 5.

3.2. Sulfur isotopes

The ratio of sulfur stable isotopes ($^{34}S/^{32}S$) was measured by elemental analyzer continuous-flow isotope-ratio mass spectrometry (EA-CF-IRMS), at the University of Washington's IsoLab facility. Using a Eurovector EA and Thermo Finnigan Conflo III and MAT253 isotope-ratio mass spectrometer.

All stable isotope ratios for samples are reported in standard delta (δ) notation indicating the per mille (‰) difference from a standard:

$$\delta = (R_{sample}/R_{std}-1) \times 1000$$

where R equals $^{34}S/^{32}S$ of the standard or sample. The standard used for sulfur isotopes is Vienna Canyon Diablo Troilite (VCDT). The accuracy of ^{34}S measurements (1σ = 0.2‰, n = 20) was estimated through analysis of NIST NBS127 and NZ1 reference materials. Analytical precision (1σ) was determined based on replicates of an internal laboratory standard (Sigma Aldrich $BaSO_4$) during each run and was ≤0.2‰ (n = 5 to 10). The average precision (1σ) for sample duplicates was larger (0.6‰, n = 2-3), probably owing to sample heterogeneity.

Sulfur concentrations were also calculated for each sample by calibrating the total S signal for a range of masses of the internal standard during each isotopic analysis. In order to identify the relative contributions of different sulfur species (sulfates including carbonate associated sulfates, sulfides, organic sulfur, and barite) to total sulfur, different sample fractions were obtained by chemical processing. Sulfates were removed from sample aliquots by an acidification step, i.e., washing with an HCl solution (2N hydrochloric acid, 36-72 hours at 60°C), leaving only sulfide and organic S in the residue. An aliquot of the residue was then bleached, i.e., treated with a 5.5% NaClO solution (12-24h, 60°C) to

remove organic sulfur, leaving only the sulfide component, although some of the sulfide fraction may have been removed by this oxidation step. An aliquot of this second residue was then treated with a nitric acid wash (6N HNO_3, 24-48h, 60°C) in order to oxidize sulfides and isolate a possible barite component.

3.3. Re-Os isotopes

The Re-Os analytical protocol followed that described in detail by Selby and Creaser (2003) and Selby et al. (2007) and was carried out in the TOTAL Laboratory for Source Geochronology and Geochemistry at Durham University. Re was recovered by anion chromatography and further purified using single anion bead chromatography. The Re and Os isolates were analyzed for their isotopic compositions by negative thermal ionization mass spectrometry. The data presented here were analyzed in two separate batch analyses. Total procedural blanks for each batch were very similar, yielding [Re] = 15.1 and 17.2 pg/g, [Os] = 150 and 193 fg/g, $^{187}Os/^{188}Os$ of 0.21 and 0.19 for the first and second batches, respectively. In-house standard solutions of Re and Os were also run and were identical to the long-term running average reported in Rooney et al. (2010 and references therein).

3.4. Trace element concentrations

The chemical composition of the samples was measured by the ALS Chemex company of Vancouver, BC (Method ME-MS61). About 0.25 g of each sample was digested in perchloric, nitric, hydrofluoric and hydrochloric acids. The residue was suspended in dilute hydrochloric acid and analyzed by inductively coupled plasma-atomic emission spectrometry (ICP-AES). Samples containing high concentrations of bismuth, mercury, molybdenum, silver, or tungsten were diluted accordingly, then analyzed by inductively coupled plasma-mass spectrometry (ICP-MS). Results were corrected for spectral

interelemental interferences. Detection limits were 0.01% by mass for most major elements and <1 ppm for most trace elements.

To control for variations in sedimentation rate and terrigenous input, elemental data were normalized to aluminum (Al), which was used as a tracer for the aluminosilicate fraction of the sediment. For ease of comparison, elemental concentrations are reported as enrichment factors (EFs), which were calculated as:

$$EF_x = (\text{wt. \% X/wt. \% Al})_{sample} / (\text{wt. \% X/wt. \% Al})_{AUCC}$$

where X is the element in question and AUCC is Average Upper Continental Crust, as determined by McLennan (2001)

3.5. Petrographic analysis

Petrographic study of a subset of samples was undertaken at the University of Cincinnati and University of Kentucky. Standard petrographic thin sections were examined at 20-400X magnification under reflected light using a Leitz Laborlux 12-Pol optical microscope. Measurements were calibrated with a Zeiss micrometer. Polished sample chips were photographed under oil-immersion lenses at varying magnifications.

4. Results

4.1. Previous isotope results

Organic carbon and nitrogen isotope datasets were generated for the Ranger Canyon and Sulphur Mountain formations at the University of Washington's IsoLab facility. Both records showed significant excursions in the lowermost SMF, with a positive peak in $\delta^{13}C_{org.}$

and a negative shift in $\delta^{15}N$. These data were previously published in Schoepfer et al., 2012 with a full description of methods and supplementary data table; the data are shown here in Figs. 3-4 for easy comparison with sulfur and trace element results.

4.2. Sulfur speciation

Average S concentrations of bulk samples (2.7±1.1%, n = 18) and acidified samples (2.7±1.2%, n = 48) (omitting sample OC24, the pyrite bed) are nearly identical. In addition, the difference between $\delta^{34}S$ for bulk and acidified extracts of the same samples is small (0.8±1.0‰, n = 18). These observations suggest a negligible contribution of sulfates to the total sulfur signal. All fully chemically processed (i.e., nitric-acid-treated) samples showed sulfur levels below detection limits or too low (<0.03 wt%) to be significant, so little if any barite is present. The bleaching step lowered sulfur levels significantly in all but one sample (OC24, the pyrite bed), often to below detection limits. With such low S levels, $\delta^{34}S$ analysis for bleached samples is much less precise, yet bleached $\delta^{34}S$ values are within +/- 5‰ of the acidified-only $\delta^{34}S$ values, a much narrower spread than for the whole data set (> 30‰). The relatively good agreement suggests the bleaching process was removing the majority of a homogenous, labile sulfur pool that may be dominated by marcasite. This suggests the acidified fraction represents an isotopically homogenous reduced sulfur pool ($S_{reduced}$, Fig. 3-4), incorporating both sulfides and organic S.

[Insert Figure 3]

[Insert Figure 4]

4.3. Sulfur concentration and isotopic profiles

Sulfur isotopes vary markedly throughout the section, and several phases can be distinguished (Figs. 3-4). In the Lower and Middle Permian, sediments are generally sulfur

poor (< 0.9 wt. %) and isotopically heavy, with $\delta^{34}S$ ranging from -5.4 to 7.2 ‰ (mean = 1.2 ‰, σ = 4.0), with the peak value 2.4 cm below the unconformity.

Heavy isotope values persist above the unconformity in the Late Permian lowermost SMF, despite much higher total sulfur content. A continuous and rapid decline in $\delta^{34}S$ can be observed between 1.5 and 29 cm (Fig. 4). This trend passes through the S wt. % maximum in the pyrite bed at ~10 cm, which has an S content of 26.4% by weight. Bleached extract for this sample yields S > 15wt% (IRMS signal saturated), and the S/Fe ratio is 1.13, nearly identical to the S/Fe ratios in pyrite (1.14), which along with field observation confirms that S in this layer is mostly in the form of pyrite. The declining isotope trend terminates in the section's $\delta^{34}S$ minimum at 29 cm ($\delta^{34}S$ = –32.0).

Above this minimum, sulfur concentrations and isotopes reach an equilibrium that they maintain for the remainder of the section. Sulfur weight % is generally at a few percent (mean = 2.3 %, σ = 1.0 %, Fig. 5) and $\delta^{34}S$ has a mean of -17.0‰ with a standard deviation of 6.0 ‰, though there is a gradual and poorly defined trend toward less negative values. There are also several minor positive excursions in $\delta^{34}S$. A small positive excursion in $\delta^{34}S$ (to –6 ‰) around 150 cm (sample OC145) is accompanied by a significant S concentration peak (6.3%).

[Insert Table 1]

[Insert Figure 5]

4.4. Petrographic data

Petrographic study revealed characteristic relationships between pyrite, organic matter, and calcite within the study samples. The basal beds (pre-LPME) of the SMF are characterized by high concentrations of sulfides in the form of massive pyrite (Fig. 6A) and large (5-50 μm), partially interlocking crystals of marcasite (Fig. 6B). These sulfides show

no relationship to primary sediment fabric; their quantity and form suggest that they may be of hydrothermal original. The beds immediately above the LPME are characterized by abundant pyrite framboids, although these framboids tend to be larger (5-10 μm; Fig. 6C) than those formed in a euxinic water column (<5 μm; Wilkin et al., 1996; Wignall and Newton, 1998). Many of the framboids show evidence of later diagenetic overgrowths (Fig. 6C-D), and blocky authigenic pyrite crystals are common (Fig. 6D-E). Higher in the section, most pyrite occurs as clusters of framboidal or blocky crystals grown either within or on the surface of large (50-500 μm) organic particles (e.g., Fig. 6G-H, L-N, P). Individual framboids in these samples are often 10-40 μm in diameter (Fig. 6H, L, O) and hence distinctly larger than syngenetic framboids (Wilkin et al., 1996). This form of pyrite is commonly associated with large, blocky calcite crystals that have grown diagenetically within the sediment (e.g., Fig. 6G-J). Blocky to massive authigenic pyrite is sometimes found in the middle of large carbonate-cemented areas without any obvious association with organic matter (e.g., Fig. 6F, K).

Several generations of carbonate are present in the sediments, including cements, with isotopic measurements indicating a diagenetic origin (Schoepfer et al. 2012). This is consistent with an increase in porewater alkalinity due to biological sulfate reduction and the inference that most of pyrite in the section formed in the sediments after deposition.

[Insert Figure 6]

4.5. Re-Os analysis

The Re-Os data are presented in Table 2. Samples collected from 20 and 30 cm above the Ranger Canyon/Sulphur Mountain unconformity are siltstone and did not contain measureable Re and Os. Between 30 and 40 cm above the unconformity the siltstone grades into black shale. The samples collected from this interval and to 1.6 m above the

unconformity are enriched in both Re and Os (~4 to 11 ppb; 78 to 157 ppt, respectively, Table 2). The $^{187}Re/^{188}Os$ range between ~240 and 400, with the $^{187}Os/^{188}Os$ being moderately radiogenic (~1.5 to 2.2). The initial $^{187}Os/^{188}Os$ (*I*Os) is calculated based on the GTS 2008 age for the Permian-Triassic boundary, 252.2 Ma (Ogg et al., 2008; Shen S.Z. et al., 2011) and the ^{187}Re decay constant of Smoliar et al. (1996). The calculated *I*Os values are shown in Figure 4. Beginning 0.4 m above the unconformity (the LPME), the *I*Os values become less radiogenic from 0.54 to 0.35. From the less radiogenic *I*Os at 0.6 m above the unconformity to 1.5m (Permian-Triassic boundary) the *I*Os values become steadily more radiogenic. At 1.6m the *I*Os trends to a less radiogenic value (~0.49).

[Insert Table 2]

4.6. Trace-element redox proxies

Certain trace elements tend to be authigenically enriched in sediments under reducing conditions, including uranium (U), vanadium (V), and molybdenum (Mo) (Algeo and Maynard, 2004; Tribovillard et al., 2006). The calculated Enrichment Factors of these elements show similar patterns (Fig. 3), suggesting that they responded to a common redox control. All three elements are highly enriched in the Johnston Canyon and Ranger Canyon Formations, with Mo and U have EFs averaging >10x their concentrations in AUCC. These values are probably indicative of sulfidic bottom water conditions throughout the deposition of these units. All three elements show steep declines in the overlying SMF, although varying somewhat in detail. V exhibits near-average values (EF ~1) throughout the SMF. Mo and U remain modestly enriched (EF <10) in the SMF, with somewhat greater enrichment in the basal 3 meters than higher in the formation. Relatively large EFs are associated with the pyrite bed at ~10 cm, where Mo has an EF of 6.8 and U has an EF of 4.1.

As euxinic water conditions will often increase the particle reactivity of redox sensitive metals, which particularly often from organo-metallic compounds (Tribovillard et al., 2006), trace element concentrations were also normalized to TOC to control for the effects of particle flux. While the actual ratios varied greatly between elements, all were generally enriched in metals relative to TOC below the unconformity, but showed strong peaks in the lowermost Sulphur Mountain Formation coincident with the pyrite bed, and remained enriched throughout the latest Permian generally.

4.7. Trace-element productivity proxies

Several trace elements sensitive to changes in organic carbon export showed significant fluctuations throughout the section. Cu, Ni, Cd, Zn, Ba, and P all show a nutrient-like distribution in seawater and are mainly transferred to sediments through sinking carbon flux. Of these, Cu, Cd, Ni, and Zn can be precipitated as sulfide minerals under euxinic or sufficiently reducing conditions, and are likely to be preserved in sediments, whereas barium is generally precipitated as barite, a sulfate, and may be released back into the water column in a regime of sulfate reduction (Dehairs et al., 1980; Averyt and Paytan, 2004). Phosphorous is mainly stored in sediments in organic matter or phosphate minerals. Under reducing conditions, phosphate may be remineralized and re-enter the water column (Meyer and Kump, 2008).

EFs were calculated for Ba, P, Cu, Ni, Cd and Zn. These elements all showed significant enrichments above AUCC in the Johnston and Ranger Canyon Formations, with P in particular being enriched above AUCC by at least a factor of 7.9 and by 2 orders of magnitude in some samples. (2 samples collected 250 and 270 cm above the unconformity saturated the ICP-AES Phosphorous peak. The maximum detectable concentration, 10^4 ppm, was used). Directly above the unconformity, P remains highly enriched with an EF of

7.6 while Zn is also extremely enriched, with a EF of 77.4, likely due to precipitation as a sulfide in the pyrite bed. Cadmium, which also forms sulfide minerals, is also orders of magnitude more enriched in this layer than the rest of the section (EF=581.4). The other elements (Ba, Cu, Ni) drop off immediately above the unconformity to values similar to AUCC, with Ba and Cu generally below an EF of 1, whereas Ni remains just above. After the pyrite bed, Zn drops off to just below average EFs similar to Cu, Ni and Ba, while P remains slightly more enriched with EFs ranging from 1 to 2.6 through the remainder of the section. EFs are shown in logarithmic scale in Figure 3.

5. Discussion

5.1. Effects of sediment mixing on geochemical signals

Reworked conodonts above the unconformity indicate that some reworking of subaerially exposed Middle Permian cherts or biological mixing of sediments has occurred. This has the potential to exercise a controlling effect on geochemical signals, especially as the resemblance of the Late Permian lowermost Sulphur Mountain to the Middle Permian Ranger Canyon in many parameters (i.e. $\delta^{15}N$, $\delta^{34}S$, several trace elements) is central to interpretation of the outcrop.

While the lowermost Sulphur Mountain shows elevated EFs in several trace elements similar to or lower than the Ranger Canyon, this is after aluminum normalization, which obscures the often higher absolute concentrations of many elements in the more aluminosilicate rich Sulphur Mountain siltstones, for example the uppermost Ranger Canyon has a measured Zn content of 19 ppm, whereas the lowermost Sulphur Mountain has 3.85 ppt, In light of this orders of magnitude variation, it would be difficult for reworking or upward mixing of Ranger Canyon material to exercise any major control on

the trace element content above the unconformity. The presence of discrete peaks in geochemical signals above the unconformity, for example the presence of an ~1 cm thick pyrite bed, the positive organic carbon isotope excursion reported in Schoepfer et al. 2012, Cd content, which spikes to 39.9 ppm at ~10 cm above the unconformity despite an average of 0.3 ppm in the Ranger Canyon Formation suggests that mixing over decimeter scales is not a controlling factor on the inorganic geochemistry of this interval.

The major isotopic shifts observed in the basal Sulphur Mountain, however, occur over smaller spatial scales, and without an independent tracer, control by mixing cannot be completely ruled out. If mixing is predominantly responsible for the heavy $\delta^{15}N$ and $\delta^{34}S$ values seen in the basal Sulphur Mountain, then the environmental changes implied by these isotopic shifts may have occurred at any time during the missing 5-7 My Lopingian interval, and may have occurred more gradually than the preserved isotope signals would suggest, however it is worth noting that Luo et al. (2011) observed abrupt nitrogen isotope shifts of similar magnitude immediately preceding the main LPME at several Tethyan sections in South China.

5.2. Benthic redox conditions

Sulfur isotopic compositions provide information about the processes of sulfide formation and, hence, paleomarine redox conditions. Syngenetic framboidal pyrite, which forms in the water column and thus from an unlimited sulfate reservoir, commonly exhibits a large negative fractionation relative to source sulfate (Goldhaber and Kaplan, 1974; Canfield and Thamdrup, 1994). In contrast, authigenic pyrite formed in the sediment exhibits heavier $\delta^{34}S$ values; if all porewater sulfate is consumed within a closed diagenetic system, the resulting sulfide will have an average $\delta^{34}S$ value equal to that of the source sulfate. The degree of shift toward heavier $\delta^{34}S$ values depends on the timing of bacterial

sulfate reduction (BSR); early BSR in a relatively open system will produce more ^{34}S-depleted sulfide than late BSR in a relatively closed system (Goldhaber and Kaplan, 1974; Chambers and Trudinger, 1979).

Modern seawater sulfate has a $\delta^{34}S$ of +20‰, yielding sulfide $\delta^{34}S$ values of about -30 to -40‰ in anoxic marine systems (Lyons, 1997; Wilkin and Arthur, 2001; Werne et al., 2003). The isotopic composition of seawater sulfate varied between +10‰ and +30‰ during the PTB transition, possibly shifting toward heavier values in the Early Triassic (Strauss, 1999; Newton and Wignall, 2004; Riccardi et al., 2006) although much variation exists within and between sections (Luo et al., 2010; Song et al., in review). Given a BSR fractionation of -30 to -60‰ (Habicht and Canfield, 2001), syngenetic pyrite in PTB sections should yield isotopic compositions between -10 and -40‰ (cf. Nielsen and Shen, 2004; Algeo et al., 2008).

Reduced sulfur $\delta^{34}S$ in the Johnston Canyon and Ranger Canyon formations average 1.0 ± 4.2‰ (n = 8). These relatively heavy values suggest precipitation in a closed system, consistent with a diagenetic origin for pyrite in this interval. The evidence of quantitative reduction of porewater sulfate in this interval despite the low organic content suggests poor postdepositional preservation may be responsible for the lack of preserved carbon despite other evidence of high productivity (see below).

The Johnston Canyon and Ranger Canyon formations contain high concentrations of V, U, and Mo. Coeval enrichments in Mo, U, and V (Fig. 3), suggest the presence of anoxic water in the Early and Middle Permian. That these enrichments are found in bioturbated sediments supporting an abundant (if homogenous) benthic fauna suggests that bottom water was oxygenated, and trace element enrichments may have resulted from a water column oxygen minimum impinging on the bottom. Coastal upwelling zones often

dynamically maintain an oxygen minimum zone (OMZ) in the mid-water column through the decomposition of sinking organic material. When the sinking flux of carbon exceeds the supply of oxygen, other electron acceptors are often used in decomposition, including nitrate and sulfate, with upwelling zones being among the primary zones of denitrification in the modern ocean (Seitzinger et al., 2006).

Nitrogen isotopes (Schoepfer et al. 2012) from Opal Creek suggest the Middle Permian upwelling system supported a mid-water oxygen minimum where denitrification and sulfate reduction were occurring. Denitrification has a substantial fractionation effect, and when it does not occur quantitatively, enriches the residual marine nitrate pool. $\delta^{15}N$ in the Ranger Canyon is consistently high, spiking to values above 9 ‰, values typically seen in modern environments where denitrification occurs in a strong water column oxygen minimum (Algeo et al. 2008).

The lower ~4 m of the SMF contains the largest concentrations of small framboids, and these beds exhibit some of the most ^{34}S-depleted values—a pattern consistent with pyrite mainly of syngenetic origin. $\delta^{34}S_{reduced}$ in the SMF averages -16.5 ± 6.8‰ (n = 47), which is distinctly higher than the isotope compositions expected for syngenetic framboidal pyrite. These compositions are consistent with pyrite formation in the diagenetic environment under quasi-open conditions, or with diagenetic overgrowths on syngenetic pyrite under somewhat more closed conditions.

TOC-S relationships are consistent with predominantly suboxic conditions during deposition of the SMF. Most samples fall along the oxic-suboxic ("normal marine") trend of Berner and Raiswell (1983; Fig. 5). A relative handful of samples, mostly in the lower ~4 m of the SMF, exhibit S concentrations considerably above those expected for oxic-suboxic facies; other evidence supports this interval having been deposited under primarily euxinic

conditions (see below). Three horizons higher in the SMF (at 4.7, 12.8, and 20.4 m) also exhibit significant S enrichment above the oxic-suboxic trendline (Fig. 5). Unlike samples from the base of the formation, however, these samples are associated with markedly heavier $\delta^{34}S$ values—an indication that the pyrite concentrations in these samples formed in the sediment and not in the water column, which is supported by petrographic data. The extinction of bioturbating benthic communities may have contribute to these intervals of near-quantitative sulfate reduction in the sediments (Shen Y. et al, 2011).

Secondary pyrite overgrowths are common in many framboidal layers, and framboid sizes are larger than those associated with syngenetic formation, especially above the basal 4 m of the SMF (Fig. 5). The observation that most framboids grew in clusters within or on the surface of large organic particles, rather than as isolated crystal aggregates, indicates a strong association of BSR with such organic substrates. The distribution of calcite within the samples, mostly as blocky diagenetic crystals adjacent to organic particles, or as "halos" enclosing these particles, is an indication that BSR within the sediment produced local increases in alkalinity that stimulated secondary carbonate precipitation (Berner, 1984).

Trace element proxies support these redox interpretations for the SMF. Mo, U, and V remain slightly enriched throughout the SMF, suggesting low oxygen conditions persisted, which along with the dearth of benthic biota, lack of bioturbation, and increased organic preservation indicate that the system transitioned to a bottom water oxygen minimum. Mo, which forms highly particle reactive oxythiomolybdates under euxinic conditions (Tribovillard et al., 2006), is particularly enriched in the lowermost 4 meters of the SMF, suggesting free sulfide in the water column during this interval.

Except for the basal ~50 cm of this formation, $\delta^{15}N$ is low and stable (Schoepfer et al. 2012, Figs. 3-4), providing no evidence of water-column denitrification as might be expected if suboxic conditions were due to high sinking fluxes of organic matter (e.g., Jenkyns et al., 2001; Algeo et al., 2008). Although the SMF consists predominantly of black shale (Munsell color), TOC values are only moderate (0.2-3.0%) yet locally higher than expected for oxic-suboxic facies (Algeo and Maynard, 2004). One explanation for this pattern may be a marked reduction in bioturbation intensity during the Early Triassic, as a consequence of the loss of most benthic infauna during the LPME (Twitchett and Wignall, 1996) and transition from a mid-water to bottom water oxygen minimum. Reduced bioturbation would severely constrain ventilation of the sediment and allow greater quantities of organic matter to be preserved for a given flux of organic matter to the sediment-water interface. Thus, multiple lines of evidence confirm that the basal ~4 m of the SMF coincided with a euxinic event, and that the remainder of the formation was deposited under oxic to suboxic conditions.

5.3. Marine circulation and productivity

The consistent enrichments in Ba, Cu, Ni, Zn, P, and Cd in the Johnson Canyon and Ranger Canyon formations are here interpreted as representing a highly productive, eutrophic marine system, despite the generally low organic carbon content of these units, which may results from poor preservation in well-ventilated bottom water. The presence of phosphate nodules in the Johnson Canyon and minor phosphatic material in the Ranger Canyon is consistent with a high-productivity environment, and the dominant fauna of the Ranger Canyon, rock-forming abundances of filter-feeding sponges, suggests a vigorous export of organic detritus from the photic zone.

High-abundance but low-diversity conodont assemblages have been suggested to indicate eutrophic conditions (Brasier, 1995), because fast-breeding species capable of rapidly exploiting the available resources tend to dominate the environment. The conodont assemblage of the Ranger Canyon Formation is dominated by high abundances of the genus *Mesogondolella*, which had a circumboreal distribution in the Middle Permian and is therefore also indicative of cold-water conditions (Henderson, 1997; Mei and Henderson, 2001).

The biota of the Johnston Canyon and Ranger Canyon formations is consistent with a high-nutrient, cold-water environment. Replacement of this prolific carbonate factory by a siliceous sponge-dominated biota occurred between the Artinskian (late Early Permian) and Guadalupian (late Middle Permian) as a consequence of climatic cooling and an increase in nutrient levels (Beauchamp and Henderson, 1994; Reid et al., 2007; Bensing et al., 2008). The high concentration of sponge-derived chert in Upper Permian beds has been interpreted as evidence of vigorous thermohaline circulation and nutrient upwelling in the Panthalassic Ocean, and its absence in Lower Triassic beds as evidence of sluggish circulation and nutrient-poor surface waters (Beauchamp, 1994; Beauchamp and Desrochers, 1997; Beauchamp and Baud, 2002). Hyalosponge facies, indicative of cold, deepwater conditions, are widespread along the western margin of Pangaea during the Early to Middle Permian, and have been used to infer the presence of coastal upwelling down to subtropical latitudes, as well as cold northern polar currents driven by sea ice in contact with the ocean (Beauchamp and Baud, 2002). Upwelling at subtropical latitudes along western Pangaea is also inferred by Ziegler et al. (1998) from sedimentological evidence, and has been modeled under a range of atmospheric conditions by Winguth and Maier-Reimer (2005).

The locality was erosive throughout most of the Lopinigian lowstand, but when

sedimentation resumed in the Changshingian the depositional environment resembled that of the Ranger Canyon in many ways. Silica sponges were still the abundant, predominant benthic fauna, although sponge spicules were increasingly diluted with siliciclastic sediments. Nitrogen and sulfur isotopes remain highly enriched, suggesting that an anoxic zone, fed by sinking organic matter and ultimately by upwelling nutrients, persisted into the latest Permian. Sediments remain bioturbated in this interval, indicating that the sea floor was relatively well oxygenated, with the oxygen minimum occurring in the water column.

~ 10 cm above the unconformity is a continuous bed containing >26% sulfur by weight, mostly in the form of pyrite, suggestive of highly euxinic water conditions, which is supported by orders-of-magnitude enrichments in the S/TOC and Mo/TOC ratios. This ~1 cm thick pyrite bed corresponds with a discrete, ~ 8 ‰ spike in organic carbon isotopes that has been interpreted as transient increase in productivity (Schoepfer et al. 2012) which may have driven the system toward euxinia, Enrichments in P, Zn, and Cd are also suggestive of enhanced productivity in this interval: while Zn and Cd are expected to complex in the sulfide sediments, P should be unaffected by euxinia and record productivity, whereas minor depletions in Barium relative to AUCC may reflect the difficulty of preserving barite ($BaSO_4$) under conditions of euxinia.

The trace element enrichments suggest that this euxinic interval may have been fueled by transient increased productivity. Numerous workers have suggested a substantial increase in continental weathering and erosion in the latest Permian (Ward et al. 2000; Sephton et al., 2005; Algeo and Twitchett, 2010; Algeo et al., 2011). This would have carried an increased complement of terrigenous nutrients, such as phosphate and iron, and may have pushed organic productivity above its already-high levels, driving the system toward euxinia.

This hypothesis receives some support from the *I*Os data (Fig. 4). The primary feature of this data set is a shift from relatively non-radiogenic values (0.35-0.40) around the LPME boundary toward more radiogenic values (~0.45 to 0.62) between 60 and 150 cm above the unconformity. This suggests that the primarily control of the Os composition in seawater during this interval (Os_{SW}) is the influx of radiogenic detritus from the cratonic continental crust (Cohen et al., 1999; Peucker-Ehrenbrink and Ravizza, 2000), into the ocean, beginning roughly with the onset of the euxinic pulse. Unradiogenic Os values seen prior to this shift may be related to the input of Os associated with the eruption of the Siberian Traps, which would be expected to possess mantle-like Os isotope signatures (~0.13-0.15; Horan et al., 1995). Values for Os_{SW} during the late Permian Arctic black shale of the Mid-Norwegian shelf yield *I*Os values of ~0.6 (Georgiev et al., 2011), which is similar to the *I*Os value of the extinction interval (~0.55) at Opal Creek, suggesting these continental weathering effects may have been widespread in the global ocean. However, in stark contrast to the Arctic black shales the $^{187}Re/^{188}Os$ values of the Opal Creek P-T section are typical of most marine organic-rich sedimentary rocks (269-394; Table 2) and therefore indicate that the conditions that permitted elevated $^{187}Re/^{188}Os$ values (~2000 to 6000) in the Arctic is regional rather than global as suggested by Georgiev et al. (2011).

The end of this intensely euxinic interval corresponds with a drop off in the previously enriched isotopes of nitrogen and sulfur. Nitrogen isotopes fall toward low values of approximately 2-3 ‰, lower than average modern marine nitrate and likely reflecting the influence of nitrogen fixation from the atmosphere in a nutrient limited environment. These low nitrogen values persist with remarkable uniformity throughout the remainder of the SMF, reflecting a new nutrient cycling regime in which water denitrification, fueled by respiration of sinking organic matter, no longer occurred on a significant scale. These changes probably reflect the collapse of vigorous coastal upwelling

and the concomitant high organic productivity that fueled anaerobic respiration in the water column.

This is supported by the collapse of all productivity-sensitive trace elements to values very near AUCC throughout the remainder of the section (excepting P and Cd, which remain slightly enriched), and by the disappearance of silica-producing sponges 30 cm above the pyrite bed, in what we interpret as corresponding to the main Permian-Triassic marine extinction. Productivity in the subsequent SMF likely reflected typical values for oligotrophic marine settings, rather than those of continental margin upwelling systems, and may have been limited by nitrogen availability, with diazotrophic prokaryotes likely playing an important role. The cessation of upwelling may have been the result of warming following the eruption of the Siberian traps, with a consequent flattening of global thermal gradients and slowing of ocean and atmospheric circulation, with both euxinia and increasing nutrient limitation playing a role in bringing about benthic extinctions in this ecosystem.

5.4. Integrated model

Here we present evidence that a coastal upwelling system, a major mode of Panthalassic ocean circulation that had persisted for tens of millions of years, abruptly terminated preceding the Permian-Triassic boundary, shifting to a relatively unproductive, nutrient limited system with suboxic to dysoxic bottom water. However, this transition was preceded by an interval of intense euxinia, corresponding to the pyrite bed and preceding the main pulse of marine extinction. This likely resulted from a transient intensification of marine productity, which may have been caused by a combination of warming climate with residual upwelling of nutrient rich waters, before the circulation slowed dramatically (Fig.

7). Higher temperatures could allow for faster algal growth and nutrient cycling, and ultimately faster and more explosive productivity. Alternatively, this pulse of high productivity may have been a global ocean scale event. The end-Permian has been linked to a change in fluvial morphology patterns, and a die off of vegetation combined with a warmer and more acidic hydrosphere following the eruption of the Siberian traps may have led to faster continental weathering and increased nutrient input into the oceans. The immaturity of siliciclastic sediments in the lowermost Sulphur Mountain Formation suggest rapid weathering was occurring. Thin pyrite beds have been found in latest Permian marine sediments along western Pangaea up into the Canadian arctic (Grasby and Beauchamp, 2009). Increased nutrient inputs may have led to one or several pulses of high productivity in latest Permian coastal oceans, driving environments to extinction-causing levels of anoxia and euxinia despite the long-term trend toward slower circulation and nutrient cycling into the Triassic.

[Insert Figure 7]

6. Conclusions

The Permian at Opal Creek records an active cold-water coastal upwelling zone that supported high productivity and a mid-water oxygen minimum zone where anaerobic respiration occurred. This system persisted for tens of millions of years only to abruptly terminate preceding the end-Permian extinction. Despite the Panthalassic Ocean's potentially dominant role in Permian biogeochemical cycling, there have been few ways to test the impact of the end-Permian crisis on circulation and ventilation. Here we present

isotopic and trace element evidence for the cessation of coastal upwelling, a modality of oceanic circulation that leaves distinctive isotopic signatures. Despite the apparent slowdown of circulation at the end Permian, a major, discrete euxinic pulse preceded the extinction, and corresponds to a number of geochemical indicators of high productivity. A transient pulse of increased carbon export may have been necessary to drive coastal oceans toward the euxinia necessary for mass extinction.

Acknowledgments

The authors would like to acknowledge the generous support provided by The United States National Science Foundation (NSF) and NASA Astrobiology Institute (NAI) University of Washington node as well as the Natural Sciences and Engineering Research Council (NSERC) of Canada, and the University of Washington Earth and Space Sciences Department. Our gratitude goes out to the staff of the University of Washington IsoLab facility for their extensive help with our isotopic analyses. TJA thanks the National Science Foundation for support (EAR-0618003, EAR-0745574, and EAR-1053449). YS would like to thank the National Natural Science Foundation of China for their support (41025011).

References

Algeo, T.J., Maynard, J.B., 2004. Trace element behavior and redox facies in core shales of Upper Pennsylvanian Kansas-type cyclothems. Chemical Geology 206, 289-318.

Algeo, T.J., Chen, Z.Q., Fraiser, M.L., Twitchett, R.J., 2011a. Terrestrial-marine teleconnections in the collapse and rebuilding of Early Triassic marine ecosystems. Palaeogeography, Palaeoclimatology, Palaeoecology 308, 1-11.

Algeo, T., Henderson, C., Ellwood, B., Rowe, H., Elswick, E., Bates, S., Lyons, T., Hower, J.C., Smith, C., Maynard, J.B., Hays, L., Summons, R., Fulton, J., Freeman, K., 2012. Evidence for a diachronous Late Permian marine crisis from the Canadian Arctic region. Geological Society of America Bulletin, in press.

Algeo, T.J., Hinnov, L., Moser, J., Maynard, J.B., Elswick, E., Kuwahara, K., Sano, H., 2010. Changes in productivity and redox conditions in the Panthalassic Ocean during the latest Permian. Geology 38, 187-190; doi:10.1130/G30483.1.

Algeo, T.J., Kuwahara, K., Sano, H., Bates, S., Lyons, T., Elswick, E., Hinnov, L., Ellwood, B., Moser, J., Maynard, J.B., 2011b. Spatial variation in sediment fluxes, redox conditions, and productivity in the Permian-Triassic Panthalassic Ocean, Palaeogeography, Palaeoclimatology, Palaeoecology 308, 65-83 doi: 10.1016/j.palaeo.2010.07.007

Algeo, T., Rowe, H., Hower, J.C., Schwark, L., Herrmann, A., Heckel, P., 2008. Changes in ocean denitrification during Late Carboniferous glacial-interglacial cycles. Nature Geoscience 1, 709-714; doi:10.1038/ngeo307.

Algeo, T.J., Shen, Y., Zhang, T., Lyons, T., Bates, S., Rowe, H., Nguyen, T.K.T., 2008. Association of ^{34}S-depleted pyrite layers with negative carbonate δ^{13}C excursions at the Permian-

Triassic boundary: Evidence for upwelling of sulfidic deep-ocean water masses. Geochemistry Geophysics Geosystems 9, Q04025, 10 pp.

Algeo, T.J., and Twitchett, R.J., 2010. Anomalous Early Triassic sediment fluxes due to elevated weathering rates and their biological consequences. Geology 38, 1023-1026.

Algeo, T.J., Wilkinson, B.H., Lohmann, K.C, 1992. Meteoric-burial diagenesis of Pennsylvanian carbonate: water/rock interactions and basin geothermics. Journal of Sedimentary Petrology 62, 652-670.

Averyt, K.B., Paytan, A., 2004. A comparison of multiple proxies for export production in the equatorial Pacific. Paleoceanography 19, PA4003, 14 pp.

Baublys, K. A., Golding, S. D., Young, E. and Kamber, B. S. (2004), Simultaneous determination of $\delta^{33}S_{V\text{-}CDT}$ and $\delta^{34}S_{V\text{-}CDT}$ using masses 48, 49 and 50 on a continuous flow isotope ratio mass spectrometer. Rapid Communications in Mass Spectrometry, 18: 2765–2769

Baud, A., Magaritz, M., Holser, W.T., 1989. Permian–Triassic of the Tethys: carbon isotope studies. Geologische Rundschau 78, 649–677.

Beauchamp, B., 1994. Permian climatic cooling in the Canadian Arctic, in Klein, G.D., ed., Pangea: Paleoclimate, Tectonics and Sedimentation during Accretion, Zenith and Break-up of a Super-Continent. Geological Society of America Special Paper 288, pp. 229-246.

Beauchamp, B., Baud, A., 2002. Growth and demise of Permian biogenic chert along northwest Pangea: evidence for end-Permian collapse of thermohaline circulation. Palaeogeography, Palaeoclimatology, Palaeoecology 184, 37-63.

Beauchamp, B., Desrochers, A., 1997. Permian warm- to very cold carbonates and cherts in northwest Pangea. In: James, N.P., Clarke, J. (eds.), Cool Water Carbonates. Society of Economic Geologists and Paleontologists Special Publication 56, pp. 327-347.

Beauchamp, B., Henderson, C.M., 1994. The Lower Permian (Artinskian) Raanes, Great Bear Cape, and Trappers Cove formations, Sverdrup Basin, Canadian Arctic: Stratigraphy and conodont zonation. Bulletin of Canadian Petroleum Geology 42, 565-600.

Beauchamp, B., Henderson, C.M., Grasby, S.E., Gates, L.T., Beatty, T.W., Utting, J., James, N.P. 2009. Late Permian sedimentation in the Sverdrup Basin, Canadian Arctic: the Lindström and Black Stripe Formations. Bulletin of Canadian Petroleum Geology 57, 167-191.

Becker, L., Poreda, R.J., Hunt, A.G., Bunch, T.E., Rampino, M. 2001. Impact event at the Permian-Triassic boundary: evidence from extraterrestrial noble gases in fullerenes. Science 291, 1530-1533.

Bensing, J.P., James, N.P., Beauchamp, B., 2008. Carbonate deposition during a time of mid-latitude ocean cooling: Early Permian “subtropical” sedimentation in the Sverdrup Basin, Arctic Canada. Journal of Sedimentary Research 78, 2-15.

Benton, M.J., Tverdokhlebov, V.P, Surkov, M.V., 2004. Ecosystem remodeling among vertebrates at the Permian-Triassic boundary in Russia. Nature 432, 97-100.

Benton, M.J., Twitchett, R.J., 2003. How to kill (almost) all life: the end-Permian extinction event. Trends in Ecology and Evolution, 18 No.7 July 2003.

Berner, R.A., 1984. Sedimentary pyrite formation: an update. Geochimica et Cosmochimica Acta 48, 605-615.

Berner, R.A., 2002. Examination of hypotheses for the Permo-Triassic boundary extinction by carbon cycle modeling. Proceedings of the National Academy of Sciences (U.S.A.) 99, 4172-4177.

Berner, R.A., Kothavala, Z., 2001. GEOCARB III: a revised model of atmospheric CO_2 over Phanerozoic time. American Journal of Science 301, 182-204.

Berner, R.A., Raiswell, R., 1983. Burial of organic carbon and pyrite sulfur in sediments over Phanerozoic time: a new theory. Geochimica et Cosmochimica Acta 47, 855-862.

Bottjer, D.J., Clapham, M.E., Frasier, M.L., Powers, C.M., 2008. Understanding mechanisms for the end-Permian mass extinction and the protracted Early Triassic aftermath and recovery. GSA Today 18, 4-10.

Brasier, M.D., 1995. Fossil indicators of nutrient levels, 1. Eutrophication and climate change. Geological Society of London Special Publications 83, pp. 113-132.

Brookfield, M.E., Twitchett, R.J., Goodings, C., 2003. Palaeoenvironments of the Permian Triassic transition sections in Kashmir, India. Palaeogeography, Palaeoclimatology, Palaeoecology 198, 353-371.

Canfield, D.E., Thamdrup, B., 1994. The production of ^{34}S-depleted sulfide during bacterial disproportionation of elemental sulfur. Science 266, 1973-1975

Chambers, L.A., Trudinger, P.A., 1979. Microbiological fractionation of stable sulfur isotopes: A review and critique. Geomicrobiological Journal 1, 249-293.

Chen, J., Beatty, T.W., Henderson, C.M., Rowe, H., 2009. Conodont biostratigraphy across the Permian-Triassic boundary at the Dawen section, Great Bank of Guizhou, Guizhou Province, South China: Implications for the Late Permian extinction and correlation with Meishan. Journal of Asian Earth Sciences 36, 442-458.

Clark, D.L., 1959. Conodonts from the Triassic of Nevada and Utah. Journal of Paleontology 33, 305-312.

Cohen, A. S., Coe, A. L., Bartlett, J. M., Hawkesworth, C. J., 1999: Precise Re-Os ages of organic-rich mudrocks and the Os isotope composition of Jurassic seawater. Earth and Planetary Science Letters 167, 159-173.

Dehairs, F., Chesselet, R., Jedwab, J., 1980. Discrete suspended particles of barite and the barium cycle in the open ocean. Earth and Planetary Science Letters 49, 528-550.

Erwin, D.H., Bowring, S.A., Jin, Y.-G., 2002. End-Permian mass-extinctions: A review. In: Koeberl, C., MacLeod, K.G. (Eds.), Catastrophic Events and Mass Extinctions: Impacts and Beyond. Geological Society of America Special Paper 356, pp. 353-383.

Fraiser, M.L., Bottjer, D.J., 2007. Elevated atmospheric CO_2 and the delayed biotic recovery from the end-Permian mass extinction. Palaeogeography, Palaeoclimatology, Palaeoecology 252, 164-175.

Fry, B., Silva, S. R., Kendall, C., Anderson, R. K. (2002), Oxygen isotope corrections for online $\delta^{34}S$ analysis. Rapid Communications in Mass Spectrometry, 16: 854–858

Gates, L.M., James, N.P., Beauchamp, B., 2004. A glass ramp: Shallow-water Permian spiculitic chert sedimentation, Sverdrup Basin, Arctic Canada. Sedimentary Geology 168, 125-147.

Georgiev, S., Stein, H.J., Hannah, J.L., Bingen, B., Weiss, H.M., Piasecki, S. 2011. Hot acidic Late Permian seas stifle life in record time. Earth and Planetary Science Letters 310, 389-400.

Gibson, D.W., 1969. Triassic stratigraphy of the Bow River-Crowsnest Pass region, Rocky Mountains of Alberta and British Columbia. Geological Survey of Canada, Paper 68, 29, 48.

Gibson, D.W., 1974. Triassic rocks of the Southern Canadian Rocky Mountains. Geological Survey of Canada, Bulletin 230, 65.

Gibson, D.W., Barclay, J.E., 1989. Middle Absaroka Sequence, The Triassic Stable Craton. In: Ricketts, B. (ed.) Basin Analysis --The Western Canada Sedimentary Basin, Canadian Society of Petroleum Geologists Special Publication, pp. 219-231.

Goldhaber, M.B., Kaplan I.R., 1974. The sulfur cycle. In: Goldberg, E.D. (ed.), The Sea, vol. 5. Wiley, pp. 569-655.

Grasby, S.E., Beauchamp, B., 2009. Latest Permian to Early Triassic basin-to-shelf anoxia in the Sverdrup Basin, Arctic Canada. Chemical Geology 264, 232-246.

Grice, K., Cao, C., Love, G.D., Bottcher, M.E., Twitchett, R.J., Grosjean, E., Summons, R.E., Turgeon, S.C., Dunning, W., Jin, Y., 2005. Photic zone euxinia during the Permian-Triassic superanoxic event. Science 307, 706-709.

Habicht, K.S., Canfield, D.E., 2001. Isotope fractionation by sulfate-reducing natural populations and the isotopic composition of sulfide in marine sediments. Geology 29, 555-558.

Haq, B.U., Schutter, S.R., 2008. A chronology of Paleozoic sea-level changes. Science 322, 64–68.

Hays, L.E., Beatty, T., Henderson, C.M., Love, G.D., Summons, R.E., 2007. Evidence for photic zone euxinia through the end-Permian mass extinction in the Panthalassic Ocean (Peace River Basin, Western Canada). Palaeoworld 16, 39-50.

Henderson, C.M., 1989. Absaroka Sequence - The Lower Absaroka Sequence: Upper Carboniferous and Permian (Chapter 10). In: Ricketts, B. (ed.) Basin Analysis - The Western Canada Sedimentary Basin, Canadian Society of Petroleum Geologists Special

Publication, pp. 203-217.

Henderson, C.M., 1997. Uppermost Permian conodonts and the Permian-Triassic boundary in the Western Canada Sedimentary Basin. Bulletin of Canadian Petroleum Geology 45, 693-707.

Henderson, C.M., Baud, A., 1997. Correlation of the Permian-Triassic boundary in Arctic Canada and comparison with Meishan, China, in Proceedings of the 30th International Geological Congress, v. 11, VSP Scientific Publishers, pp. 143-152.

Henderson, C.M., 2006. Beware of your FO and be aware of the FAD. Permophiles 47, 8-9.

Henderson, C.M., Mei, S., 2007. Geographical clines in Permian and Lower Triassic gondolellids and its role in taxonomy. Palaeoworld 16, 190-201.

Henderson, C.M., Richards, B.C., Barclay, J.E., 1994. Permian. In: Mossop, G.D. (ed.) Geological Atlas of the Western Canada Sedimentary Basin Joint publication of the Canadian Society of Petroleum Geologists and the Alberta Research Council, pp. 251-258.

Horan, M.F., Walker, R.J., Fedorenko, V.A., Czamanske, G.K. 1995. Osmium and neodymium isotopic constraints on the temporal and spatial evolution of Siberian flood basalt sources. Geochimica et Cosmochimica Acta 59, 5159–5168

Hotinski, R.M., Bice, K.L., Kump, L.R., Najjar, R.G., Arthur, M.A., 2001. Ocean stagnation and end-Permian anoxia. Geology 29, 7-10.

Huey, R.B., Ward, P.D., 2005. Hypoxia, global warming, and terrestrial Late Permian extinctions. Science 308, 398-401.

Hunt, J.M., 1996. Petroleum Geochemistry and Geology, 2nd ed., W.H. Freeman, New York, 743 pp.

Isozaki, Y., 1994. Superanoxia across the Permo–Triassic boundary: record in accreted

deep-sea pelagic chert in Japan. In: Embry, A.F., Beauchamp, B., Glass, D.J. (eds.), Pangea: Global Environments and Resources. Canadian Society of Petroleum Geologists, Memoir, vol. 17, pp. 805–812.

Isozaki, Y., 1997. Permo-Triassic boundary superanoxia and stratified superocean: records from lost deep-sea. Science 276, 235-238.

Isozaki, Y., Kawahata, H., Ota, A., 2007. A unique carbon isotope record across the Guadalupian-Lopingian (Middle-Upper Permian) boundary in mid-oceanic paleo-atoll carbonates: The high-productivity "Kamura event" and its collapse in Panthalassa. Global and Planetary Change 55, 21-38.

Jenkyns, H.C., Gröcke, D.R., Hesselbo, S.P., 2001. Nitrogen isotope evidence for water mass denitrification during the early Toarcian (Jurassic) oceanic anoxic event. Paleoceanography 16, 593-603.

Jiang, H., Lai, X., Luo, G., Aldridge, R., Zhang, K., Wignall, P., 2007. Restudy of conodont zonation and evolution across the P/T boundary at Meishan section, Changxing, Zhejiang, China. Global and Planetary Change 55, 39-55.

Jin, Y.G., Wang, Y., Wang, W., Shang, Q.H., Cao, C.Q., Erwin, D.H., 2000. Pattern of marine mass extinction near the Permian Triassic boundary in South China. Science 289, 432-436.

Kashiyama Y., Ogawa, N.O., Kuroda, J., Shiro M., Nomoto S., Tada R., Kitazato H., Ohkouchi N., 2008. Diazotrophic cyanobacteria as the major photoautotrophs during mid-Cretaceous oceanic anoxic events: Nitrogen and carbon isotopic evidence from sedimentary porphyrin. Organic Geochemistry 39, 532-549.

Kidder, D.L., Worsley, T.R., 2003. Late Permian warming, the rapid latest Permian transgression, and the Permo-Triassic extinction, 2003 GSA Annual Meeting: Seattle,

WA.

Kidder, D.L., Worsley, T.R., 2004. Causes and consequences of extreme Permo-Triassic warming to globally equable climate and relation to the Permo-Triassic extinction and recovery. Palaeogeography, Palaeoclimatology, Palaeoecology 203, 207-237.

Kiehl, J.T., Shields, C.A., 2005. Climate simulation of the latest Permian: implications for mass extinction. Geology 33, 757-760.

Kim, S.T., O'Neil, J. R.. 1997. Equilibrium and nonequilibrium oxygen isotope effects in synthetic carbonates. Geochimica et Cosmochimica Acta 61, 3461-3475.

Knoll, A.H., Bambach, R.K., Canfield, D.E., Grotzinger, J.P., 1996. Comparative Earth history and Late Permian mass extinction. Science 273, 452-457.

Korte, C., Kozur, H.W., 2010. Carbon-isotope stratigraphy across the Permian-Triassic boundary: A review. Journal of Asian Earth Sciences, doi:10.1016/j.jseaes.2010.01.005

Korte, C., Pande, P., Kalia, P., Kozur, H.W., Joachimski, M., Oberhänsli. H., 2010. Massive volcanism at the Permian–Triassic boundary and its impact on the isotopic composition of the ocean and atmosphere. Journal of Asian Earth Sciences 37, 293-311.

Kozur, H.W., 2005. Pelagic uppermost Permian and Permian-Triassic boundary conodonts of Iran. Part II: investigated sections and evaluation of the conodont faunas. Hallesches Jahrbuch Fur Geowissenschaften, Reihe B: Geologie, Palaontologie, Mineralogie, 19, 49-86.

Krull, E.S., Retallack, G.J., Campbell, H.J., Lyon, G.L.., 2000. $\delta^{13}C_{org}$ chemostratigraphy of the Permian-Triassic boundary in the Maitai Group, New Zealand: Evidence for high-latitudinal methane release. New Zealand Journal of Geology and Geophysics 43, 21-32.

Kump, L.R., Pavlov, A., Arthur, M.A., 2005. Massive release of hydrogen sulfide to the surface ocean and atmosphere during interval of oceanic anoxia. Geology 33, 397-400.

Looy, C.V., Twitchett, R.J., Dilcher, D.L., van Konijnenburg-van Cittert, J.H.A., Visscher, H., 2001. Life in the end-Permian dead zone. Proceedings of the National Academy of Sciences (U.S.A.) 98, 7879-7883.

Luo, G., Kump, L.R., Wang, Y., Tong, J., Arthur, M.A., Yang, H., Huang, J., Yin, H., Xie, S., 2010. Isotopic evidence for an anomalously low oceanic sulfate concentration following end-Permian mass extinction. Earth and Planetary Science Letters 300, 101-111.

Luo, G., Wang, Y., Kump, L.R., Bai, X., Algeo, T.J., Yang, H., Xie, S., 2011. Nitrogen fixation prevailed simultaneously with the end-Permian marine mass extinction and its implications. Geology, v. 39, p. 647-650.

Luo, G., Wang, Y., Yang, H., Algeo, T.J., Kump L.R., Huang, J., Xie, S., 2011. Stepwise and large-magnitude negative shift in $\delta^{13}C_{carb}$ preceded the main marine mass extinction of the Permian-Triassic crisis interval. Palaeogeography, Palaeoclimatology, Palaeoecology 299, 70-82.

Lyons, T.W., 1997. Sulfur isotopic trends and pathways of iron sulfide formation in upper Holocene sediments of the anoxic Black Sea. Geochimica et Cosmochimica Acta 61, 3367-3382.

McLennan, S.M., 2001. Relationships between the trace element composition of sedimentary rocks and upper continental crust. Geochemistry Geophysics Geosystems, 2, GC000109, 24 pp.

Mei, S., 1996. Restudy of conodonts from the Permian-Triassic boundary beds at Selong and Meishan and the natural Permian-Triassic boundary. In: Wang, H. and Wang, X. (eds.).

Memorial Volume of Prof. Sun Yunzhu: Palaeontology and Stratigraphy. Centennial China University of Geosciences Press, Wuhan, pp. 141-148.

Mei, S., Henderson, C.M. 2001. Evolution of Permian conodont provincialism and its significance in global correlation and paleoclimatic implication. Palaeogeography, Palaeoclimatology, Palaeoecology 170, 237-260.

Mei, S.L., Zhang, K.X., Wardlaw, B.R., 1998. A refined succession of Changhsingian and Griesbachian neogondolellid conodonts from the Meishan section, candidate of the global stratotype section and point of the Permian-Triassic boundary. Palaeogeography, Palaeoclimatology, Palaeoecology 143, 213-226.

Meyer, K.M., Ridgwell, A., and Kump, L.R., 2008. Biogeochemical controls on photic zone euxinia during the end-Permian mass extinction. Geology 36(9), 747-750.

Meyer, K.M., Kump, L.R., 2008. Oceanic euxinia in Earth history: Causes and consequences. Annual Review of Earth and Planetary Sciences 36, 251-288.

Meyer, K.M., Yu, M., Jost, A.B., Kelley, B.M., Payne, J.L., 2011. $\delta^{13}C$ evidence that high primary productivity delayed recovery from end-Permian mass extinction. Earth and Planetary Science Letters 302, 378-384.

Musashi, M., Isozaki, Y., Koike, T., Kreulen, R., 2001. Stable carbon isotope signature in mid-Panthalassa shallow-water carbonates across the Permo-Triassic boundary: evidence for ^{13}C-depleted superocean. Earth and Planetary Science Letters 191, 9-20.

Newton, R.J., Pevitt, E.L., Wignall, P.B., Bottrell, S.H., 2004. Large shifts in the isotopic composition of seawater sulphate across the Permo-Triassic boundary in northern Italy. Earth and Planetary Science Letters 218, 331-345.

Nielsen, J.K., Shen, Y., 2004. Evidence for sulfidic deep water during the Late Permian in the East Greenland Basin. Geology 32, 1037-1040.

Ogg, J. G., Ogg, G., Gradstein, F.M. 2008. The Concise Geologic Time Scale, Cambridge University Press

O'Leary, M.H., 1981. Carbon isotope fractionation in plants. Phytochemistry 20, 553-567.

O'Leary, M. H., 1988. Carbon isotopes in photosynthesis. Bioscience 38, 328-336.

Orchard, M.J., Krystyn, L., 1998. Conodonts of the lowermost Triassic of Spiti, and new zonation based on Neogondolella successions. Revista Italiana di Paleontologia Stratigraphia 104 (3), 341-368.

Orchard, M.J., Nassichuk, W.W., Rui, L., 1994. Conodonts from the Lower Griesbachian Otoceras latilobatum bed of Selong, Tibet and the position of the P-T boundary. Canadian Society of Petroleum Geologists. Proceedings of Pangea Conference Memoir, vol. 17, pp. 823-843.

Payne, J.L., Kump, L.R., 2007. Evidence for recurrent Early Triassic massive volcanism from quantitative interpretation of carbon isotope fluctuations. Earth and Planetary Science Letters 256, 264-277.

Payne, J.L., Lehrmann, D.J., Wei, J., Orchard, M.J., Schrag, D.P., Knoll, A.H., 2004. Large perturbations of the carbon cycle during recovery from the end-Permian extinction. Science 305, 506-509.

Peucker-Ehrenbrink, B., Ravizza, G., 2000. The marine osmium isotope record. Terra Nova 12, 205-219.

Radke, M., Welte, D.H., Willsch, H., 1982. Geochemical study on a well in the Western Canada Basin: relation of the aromatic distribution pattern to maturity of organic matter.

Geochimica et Cosmochimica Acta 46, 1-10.

Raup, D.M., Sepokoski, J.J., 1982. Mass extinction in the marine fossil record. Science 215, 1501-1503.

Reichow, M.K., Pringle, M.S., Al'Mukhamedov, A.I., Allen, M.B., Andreichev, V.L., Buslov, M.M., Davies, C.E., Fedoseev, G.S., Fitton, J.G., Inger, S., Medvedev, A.Y., Mitchell, C., Puchkov, V.N., Safanova, I.Y., Scott, R.A., Saunders, A.D., 2009. The timing and extent of the eruption of the Siberian Traps large igneous province: Implications for the end-Permian environmental crisis. Earth and Planetary Science Letters 277, 9-20.

Reid, C.M., James, N.P., Beauchamp, B., Kyser, T.K., 2007. Faunal turnover and changing oceanography: late Palaeozoic warm-to-cool water carbonates, Sverdrup Basin, Canadian Arctic Archipelago. Palaeogeography, Palaeoclimatology, Palaeoecology 249, 128-159.

Retallack, G.J., 1999. Postapocalyptic greenhouse paleoclimate revealed by earliest Triassic paleosols in the Sydney Basin, Australia. Geol. Soc. Am. Bull. 111, 52-70.

Retallack, G.J., Jahren, A.H., 2008. Methane release from igneous intrusion of coal during Late Permian extinction events. Journal of Geology 116, 1-20.

Retallack, G.J., Smith, R.M.H., Ward, P.D., 2003. Vertebrate extinction across the Permian–Triassic boundary in Karoo Basin, South Africa. Geological Society of America Bulletin 115, 1133-1152.

Riccardi, A.L., Arthur, M.A., Kump, L.R., 2006. Sulfur isotopic evidence for chemocline upward excursions during the end-Permian mass extinction. Geochimica et Cosmochimica Acta 70, 5740-5752.

Richards, B.C., 1989. Upper Kaskaskia Sequence: Uppermost Devonian and Lower Carboniferous. In: Ricketts, B. (ed.) Basin Analysis - The Western Canada Sedimentary Basin, Canadian Society of Petroleum Geologists Special Publication, pp. 165-201.

Rooney, A.D., Selby, D., Houzay, J-P., Renne, P.R., 2010. Re-Os geochronology of Mesoproterozoic sediments from the Taoudeni basin, Mauritania: Implications for basin-wide correlations, supercontinent reconstruction and Re-Os systematics of organic-rich sediments. Earth and Planetary Science Letters 289, 486-496.

Sano, H., Kuwahara, K., Yao, A., Agematsu, S., 2010. Panthalassic seamount-associated Permian-Triassic boundary siliceous rocks, Mino terrane, central Japan. Paleontological Research 14, 293-314.

Schoepfer, S.D., Henderson, C.M., Garrison, G.H., Ward, P.D. 2012 Cessation of a productive coastal upwelling system in the Panthalassic Ocean at the Permian–Triassic Boundary, Palaeogeography, Palaeoclimatology, Palaeoecology 313–314, 181-188

Seitzinger, S., Harrison, J.A., Böhlke, J.K., Bouwman, A.F., Lowrance, R., Peterson, B., Tobias, C., Van Drecht, G., 2006. Denitrification across landscapes and waterscapes: a synthesis. Ecological Applications 16, 2064–2090.

Selby, D.A., Creaser, R.A., 2003. Re-Os geochronology of organic rich sediments: an evaluation of organic matter analysis methods. Chemical Geology 200, 225-240.

Selby, D. 2007. Direct rhenium-osmium age of the oxfordian-kimmeridgian boundary, Staffin Bay, Isle of Skye, UK and the Late Jurassic geologic timescale. Norwegian Journal of Geology, 87, 291-299.

Sephton, M.A., Looy, C.V., Brinkhuis, H., Wignall, P.B., de Leeuw, J.W., Visscher, H. 2005 Catastrophic soil erosion during the end-Permian biotic crisis. Geology 33, 941-944

Shen, S., Cao, C., Henderson, C.M., Wang, X., Shi, G.R., Wang, Y. and Wang, W., 2006. End-Permian mass extinction pattern in the northern peri-Gondwanan region. Palaeoworld 15, 3-30.

Shen, S.Z., Crowley, J.L., Wang, Y., Bowring, S.A., Erwin, D.H., Sadler, P.M., Cao, C.Q., Rothman, D.H., Henderson, C.M., Ramezani, J., Zhang, H., Shen, Y., Wang, X.D., Wang, W., Mu, L., Li, W.Z., Tang, Y.G., Liu, X.L., Liu, L.J., Zeng, Y., Jiang, Y.F., Jin, Y.-G. 2011. Calibrating the end-Permian mass extinction. Science 334, 1367-1372.

Shen, S.Z., Henderson, C.M., Bowring, S.A., Cao, C.Q., Wang, Y., Wang, W., Zhang, H., Zhang, Y.C., Mu, L., 2010. High-resolution Lopingian (Late Permian) timescale of South China. Geological Journal 45, 122-134.

Shen, Y., Farquhar, J., Zhang, H., Masterson, A., Zhang, T., Wing, B.A., 2011. Multiple S-isotopic evidence for episodic shoaling of anoxic water during Late Permian mass extinction. Nature Communications 2:210, 1-5.

Smoliar, M. I., Walker, J.R., Morgan, J.W. 1996. Re-Os isotope constraints on the age of Group IIA, IIIA, IVA, and IVB iron meteorites. Science 271, 1099-1102.

Song, H.Y., Tong, J.N., Algeo, T.J., Qiu, H.O., Song, H.J., Tian, L., Chen, Z.Q., in review. Large shallow-to-deep $\delta^{13}C$ gradients in Early Triassic seas of the South China craton: Evidence for elevated primary productivity and its role in sustaining oceanic anoxia and delaying marine ecosystem recovery following the end-Permian mass extinction. Global and Planetary Change, submitted October 2011.

Song, H.Y., Tong, J.N., Algeo, T.J., Song, H.J., in review. Coupling of the marine carbon and sulfur cycles during the Early Triassic. Nature Geoscience, submitted November 2011.

Strauss, H., 1999. Geological evolution from isotope proxy signals—sulfur. Chemical Geology 161, 89-101.

Sweet, W.C., 1970. Uppermost Permian and Lower Triassic conodonts of the Salt Range and Trans-Indus Ranges — West Pakistan. In: Kummel, B., Teichert, C. (eds.), Stratigraphic Boundary Problems: Permian and Triassic of West Pakistan. University of Kansas, Special Publications, vol. 4, pp. 207-275.

Taylor, E.T., Taylor, T.N., Cúeno, R., 2000. Permian and Triassic high latitude paleoclimates: evidence from fossil biotas. In: Huber, B., Macleod, K. (eds.) Warm Climates in Earth History: Cambridge, Cambridge University Press, pp. 321-350.

Tissot, B.P., Welte, D.H., 1984. Petroleum Formation and Occurrence, 2nd ed., Springer, Berlin, 699 pp.

Tribovillard, N., Algeo, T.J., Lyons, T., Riboulleau, A., 2006. Trace metals as paleoredox and paleoproductivity proxies: An update. Chemical Geology 232, 12-32.

Twitchett, R.J., Wignall, P.B., 1996. Trace fossils and the aftermath of the Permo-Triassic mass extinction: evidence from northern Italy. Palaeogeography, Palaeoclimatology, Palaeoecology 124, 137-151.

Utting, J., Zonneveld, J.P., MacNaughton, R.B., Fallas, K.M., 2005. Palynostratigraphy, lithostratigraphy and thermal maturity of the Lower Triassic Toad and Grayling, and Montney formations of western Canada, and comparisons with coeval rocks of the Sverdrup Basin, Nunavut. Bulletin of Canadian Petroleum Geology 63, 5-24.

Ward, P.D., Montgomery, D.R., Smith, R., 2000. Altered river morphology in South Africa related to the Permian-Triassic extinction. Science 289, 1740-1743.

Ward, P.D., Botha, J., Buick, R., De Kock, M.O., Erwin, D.H., Garrison, G., Kirschvink, J., Smith,

R., 2005. Abrupt and Gradual Extinction Among Late Permian Land Vertebrates in the Karoo Basin, South Africa. www.sciencexpress.org / 20 January 2005 / Page 1/ 10.1126/science.1107068.

Werne, J.P., Lyons, T.W., Hollander, D.J., Formolo, M.J., Sinninghe Damsté, J.S., 2003. Reduced sulfur in euxinic sediments of the Cariaco Basin: sulfur isotope constraints on organic sulfur formation. Chemical Geology 195, 159-179.

White, R.V., 2002. Earth's biggest 'whodunnit': unravelling the clues in the case of the end-Permian mass extinction: Philosophical Transactions of the Royal Society of London, Series B, 360, 2963-2985.

Wignall, P.B., 2007. The End-Permian mass extinction—how bad did it get? Geobiology 5, 303-309.

Wignall, P.B., Hallam, A., 1992. Anoxia as a cause of the Permian/Triassic mass extinction: facies evidence from northern Italy and the western United States. Palaeogeography, Palaeoclimatology, Palaeoecology 93, 21-46.

Wignall, P.B., Hallam, A., 1993. Griesbachian (Earliest Triassic) palaeoenvironmental changes in the Salt Range, Pakistan and southeast China and their bearing on the Permo-Triassic mass extinction. Palaeogeography, Palaeoclimatology, Palaeoecology 102, 215-237.

Wignall, P.B., Newton, R., 1998. Pyrite framboid diameter as a measure of oxygen deficiency in ancient mudrocks. American Journal of Science 298, 537-552.

Wignall, P.B., Newton, R. 2003. Contrasting deep-water records from the Upper Permian and Lower Triassic of South Tibet and British Columbia: evidence for a diachronous mass extinction. Palaios 18, 153-167.

Wignall, P.B., Twitchett, R.J., 1996. Oceanic anoxia and the end Permian mass extinction. Science 272, 1155-1158.

Wignall, P.B., Twitchett, R.J., 2002. Extent, duration, and nature of the Permian-Triassic superanoxic event. In: Koeberl, C., MacLeod, K.G. (eds.), Catastrophic Events and Mass Extinctions: Impacts and Beyond. Geological Society of America Special Paper 356, pp. 395-413.

Wilkin, R.T., Arthur, M.A., 2001. Variations in pyrite texture, sulfur isotope composition, and iron systematics in the Black Sea: Evidence for late Pleistocene to Holocene excursions of the O2-H2S redox transition. Geochimica et Cosmochimica Acta 65, 1399-1416.

Wilkin, R.T., Barnes, H.L., Brantley, S.L., 1996. The size distribution of framboidal pyrite in modern sediments: an indicator of redox conditions. Geochimica et Cosmochimica Acta 60, 3897-3912.

Winguth, A.M.E., Heinze, C., Kutzbach, J. E., Maier-Reimer, E., Mikolajewicz, U., Rowley, D., Rees, A., and Ziegler, A. M., 2002. Simulated warm polar currents during the middle Permian, Paleoceanography 17(4), 1057, doi:10.1029/2001PA000646.

Winguth, A.M.E., Maier-Reimer, E., 2005. Causes of marine productivity and oxygen changes associated with the Permian-Triassic boundary: A reevalution with ocean general circulation models. Marine Geology 217, 283-304.

Yin, H.F., Sweet, W.C., Glenister, B.F., Kotlyar, G., Kozur, H., Newell, N.D., Sheng, J.Z., Yang, Z.Y., Zakharov, Y.D., 1996. Recommendation of the Meishan section as Global Stratotype Section and Point for basal boundary of Triassic system. Newsletter on Stratigraphy 34, 81-108.

Yin, H.F., Zhang, K.X., Tong, J.N., Yang, Z.Y., Wu, S.B., 2001. The Global Stratotype Section and Point (GSSP) of the Permian–Triassic boundary. Episodes 24, 102-114.

Zhang, K., Tong, J., Shi, G.R., Lai, X., Yu, J., He, W., Peng, Y., Jin, Y., 2007. Early Triassic conodont-palynological biostratigraphy of the Meishan D section in Changxing, Zhejiang Province, South China. Palaeogeography, Palaeoclimatology, Palaeoecology 252, 4-23.

Ziegler A.M., Gibbs M.T., Hulver M.L., 1998. A mini-atlas of oceanic water masses in the Permian period. Proceedings of the Royal Society of Victoria 110 (1/2), 323– 343.

Figure and Table captions

Figure 1. (A) Late Permian paleogeography, showing the major ocean basins and location of the Opal Creek section. Map generated by PaleoDB.org, Alroy 2010. (B) Map of Canada showing the location of the Kananaskis Valley in southwestern Alberta. (C) Map showing the location of the Opal Creek section in the Kananaskis Valley.

Figure 2. (A) Photograph of Opal Creek outcrop from approach. Note cliff-forming, silicified Ranger Canyon and less resistant Sulphur Mountain silts exposed in hillside. The cliff face corresponds to the unconformity. (B) Close up of Permian-Triassic boundary. Pyrite bed weathers to reddish in outcrop. RC = Ranger Canyon Formation, SM = Sulphur Mountain Formation, SB = unconformable Sequence Boundary, Py. = Pyrite layer, Ext. = main extinction horizon.

Figure 3. Stratigraphic column with lithostratigraphy as well as isotopic and trace element records for the Opal Creek section. Heavy red line corresponds to the biostratigraphic PTB, the thin red line corresponds to the main marine extinction event. The number of samples analyzed for each proxy is as follows: $\delta^{13}C_{org}$, n = 191, $\delta^{15}N$, n = 58, $\delta^{34}S$, n = 56 acidified (n = 7 acidified+bleached), %S, n = 55, TOC, n = 185, All trace element proxies, n = 29.

Figure 4. Expanded stratigraphic column for 4.5-m-thick interval of the Opal Creek section bracketing the unconformity and PTB, with isotope measurements and calculated initial osmium isotope ratios (*I*Os, see Re-Os Analysis in Results section). Solid red line indicates the biostratigraphic PTB, the dashed red line indicates the main extinction event. *M. bitteri* zone overlaps with *M. rosenkrantzi* in uppermost 5-10 cm of Ranger Canyon Formation. The number of measurements shown for each proxy is as follows: $\delta^{13}C_{org}$, n = 149, $\delta^{15}N$, n = 41, $\delta^{34}S$, n = 36 acidified (n = 2 acidified+bleached), *I*Os, n = 14.

Figure 5. (A) TOC versus total S. The majority of samples falls along the oxic-suboxic trend of Berner and Raiswell (1983). A subset of samples (n ~12) plots distinctly above the oxic-suboxic trend; they represent the basal 4 m of the SMF plus a few pyritic layers higher in the section. (B) Total S versus pyrite $\delta^{34}S$. Note that high-S samples are low in TOC and enriched in ^{34}S. Samples shown in this figure are a separate set processed at the U. of Cincinnati.

Figure 6. Reflected light petrographic photomicrographs of SMF: (A) Massive pyrite in calcareous silicate matrix. (B) Massive marcasite in silicate matrix. (C) Medium-sized (8-12 μm) pyrite framboids with partial diagenetic overgrowths. (D) Coarse euhedral and

irregular diagenetic pyrite masses. (E) Large (35 μm) pyrite framboid with diagenetic overgrowths. (F) Fine (3-10 μm) diagenetic pyrite crystals in a large organic particle. (G) Fine diagenetic pyrite within a diagenetic calcite crystal. (H) Variably sized (4-20 μm) pyrite framboids along an organic-rich lamina. (J) Coarse diagenetic pyrite associated with diagenetic carbonate crystals. (K) Coarse diagenetic pyrite within a carbonate nodule. (L) Variably sized (10-40 μm) pyrite framboids along an organic-rich lamina. (M) Organic particle with diagenetic pyrite overgrowths (lower left) and blocky diagenetic pyrite (upper right). (N) Fine (4-12 μm) pyrite framboids along an organic-rich lamina. (O) Coarse (20-40 μm) pyrite framboids with diagenetic overgrowths on larger framboid. (P) Fine (3-8 μm) diagenetic pyrite crystals in an organic particle.

Figure 7. Integrated model of environmental conditions on the subtropical eastern Panthalassic margin (A) During the Early and Middle Permian (B) During the main latest Permian extinction interval (C) During the earliest Triassic

Table 1. Concentrations and enrichment factors of some major and trace elements

†AUCC = Average Upper Continental Crust (McLennan 2001)

Table 2. Re and Os concentrations and isotopes. *I*Os uncertainties were less than or equal to .004**.**

†Initial osmium compositions (*I*Os) calculated for an age of 252.2 Ma.

Figure 1

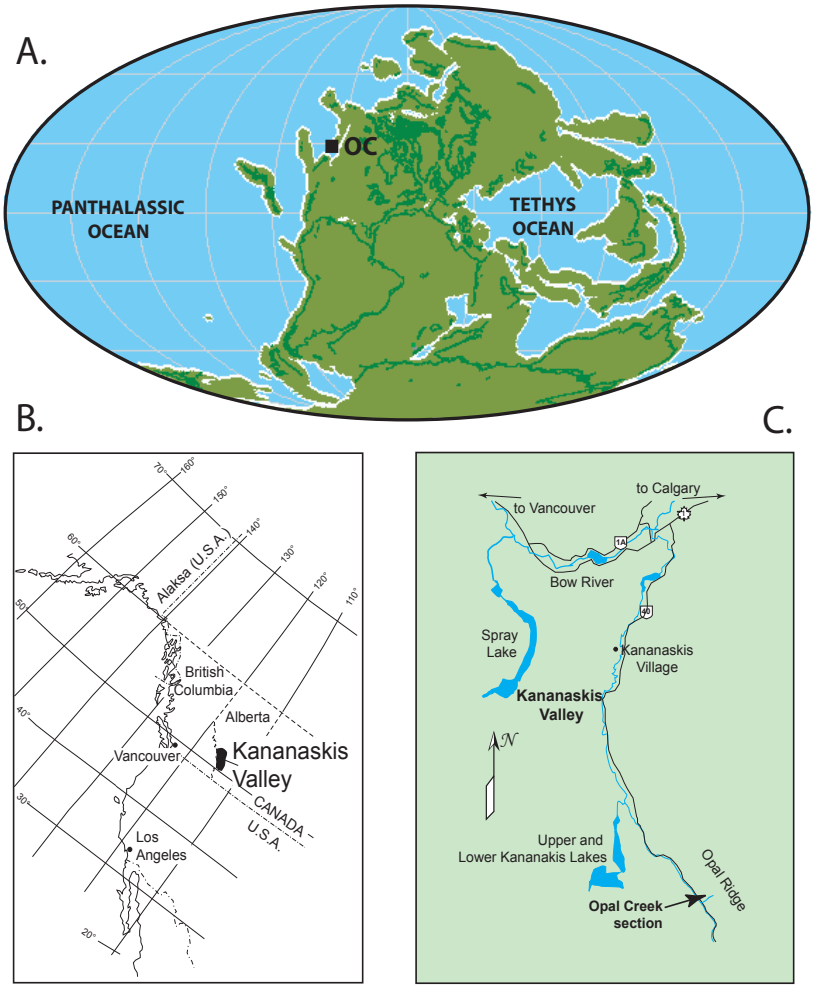
A.
OC
PANTHALASSIC OCEAN
TETHYS OCEAN
B.
Alaska (U.S.A.)
British Columbia
Alberta
Vancouver
Kananaskis Valley
CANADA
U.S.A.
Los Angeles
C.
to Vancouver
to Calgary
Bow River
Spray Lake
Kananaskis Village
Kananaskis Valley
N
Upper and Lower Kananakis Lakes
Opal Ridge
Opal Creek section

Figure 2

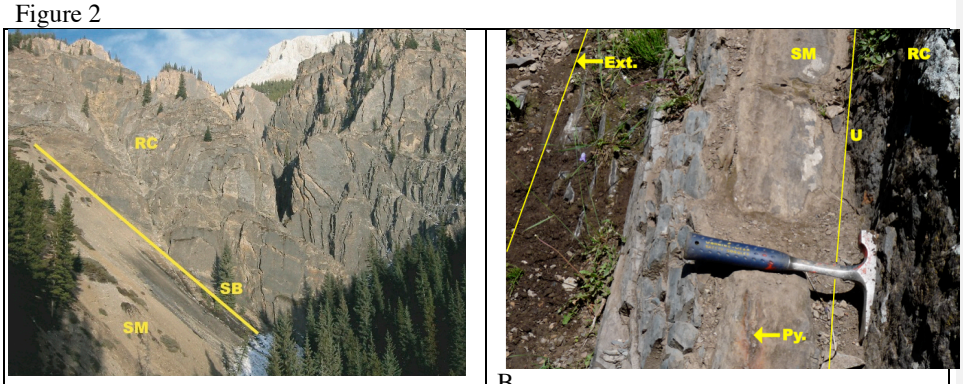

A. B.

Figure 3

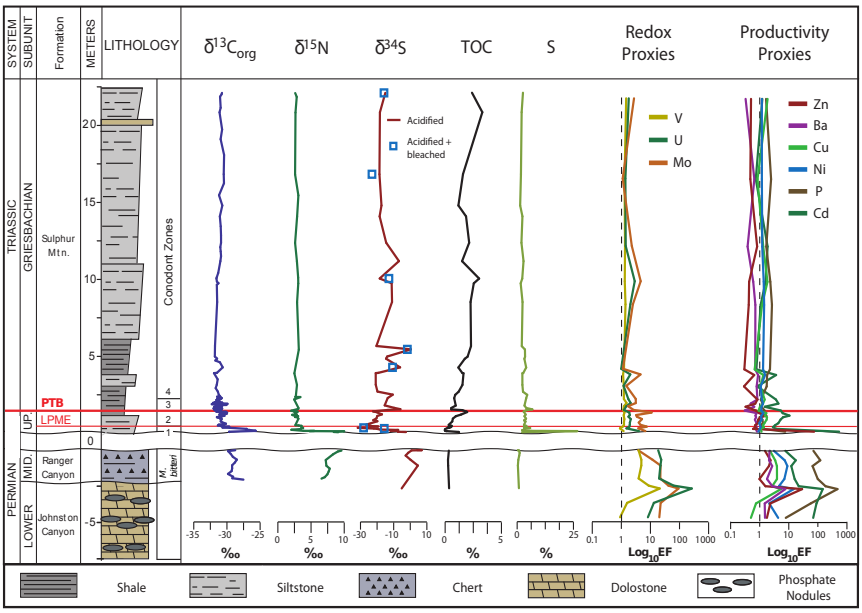
SYSTEM
SUBUNIT
Formation
METERS
LITHOLOGY
δ13Corg
δ15N
δ34S
TOC
S
Redox Proxies
Productivity Proxies
TRIASSIC
GRIESBACHIAN
Sulphur Mtn.
PTB
LPME
UP.
PERMIAN
MID.
Ranger Canyon
LOWER
Johnston Canyon
Conodont Zones
Acidified
Acidified + bleached
V
U
Mo
Zn
Ba
Cu
Ni
P
Cd
‰
‰
‰
%
%
Log10EF
Log10EF
Shale
Siltstone
Chert
Dolostone
Phosphate Nodules

Figure 4.

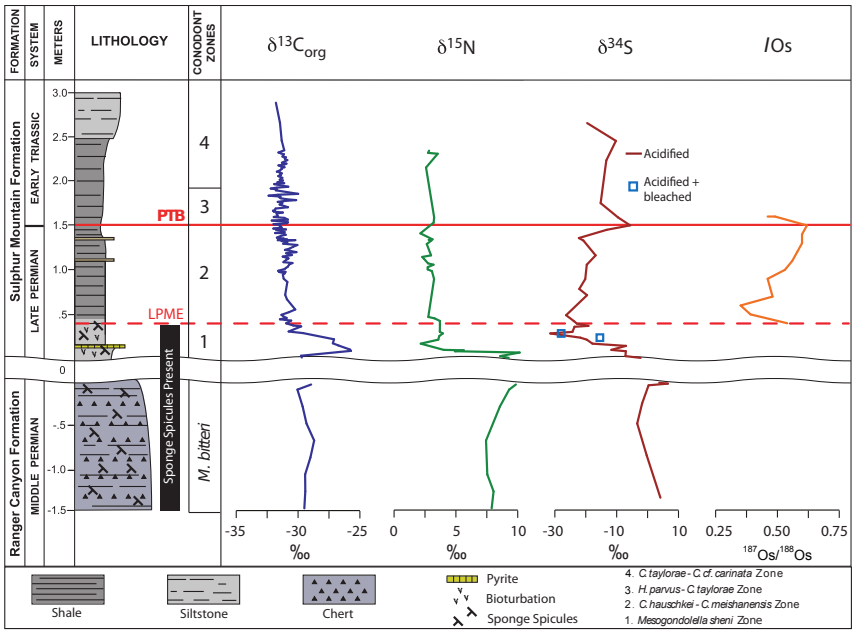
FORMATION
SYSTEM
METERS
LITHOLOGY
CONODONT ZONES
δ13Corg
δ15N
δ34S
IOs
Sulphur Mountain Formation
EARLY TRIASSIC
LATE PERMIAN
Ranger Canyon Formation
MIDDLE PERMIAN
3.0
2.5
2.0
1.5
1.0
.5
0
-.5
-1.0
-1.5
PTB
LPME
Sponge Spicules Present
4
3
2
1
M. bitteri
Acidified
Acidified + bleached
-35
-30
-25
‰
0
5
10
‰
-30
-10
10
‰
0.25
0.50
0.75
187Os/188Os
Shale
Siltstone
Chert
Pyrite
Bioturbation
Sponge Spicules
4. C.taylorae - C.cf. carinata Zone
3. H.parvus - C.taylorae Zone
2. C.hauschkei - C.meishanensis Zone
1. Mesogondolella sheni Zone

Figure 5.

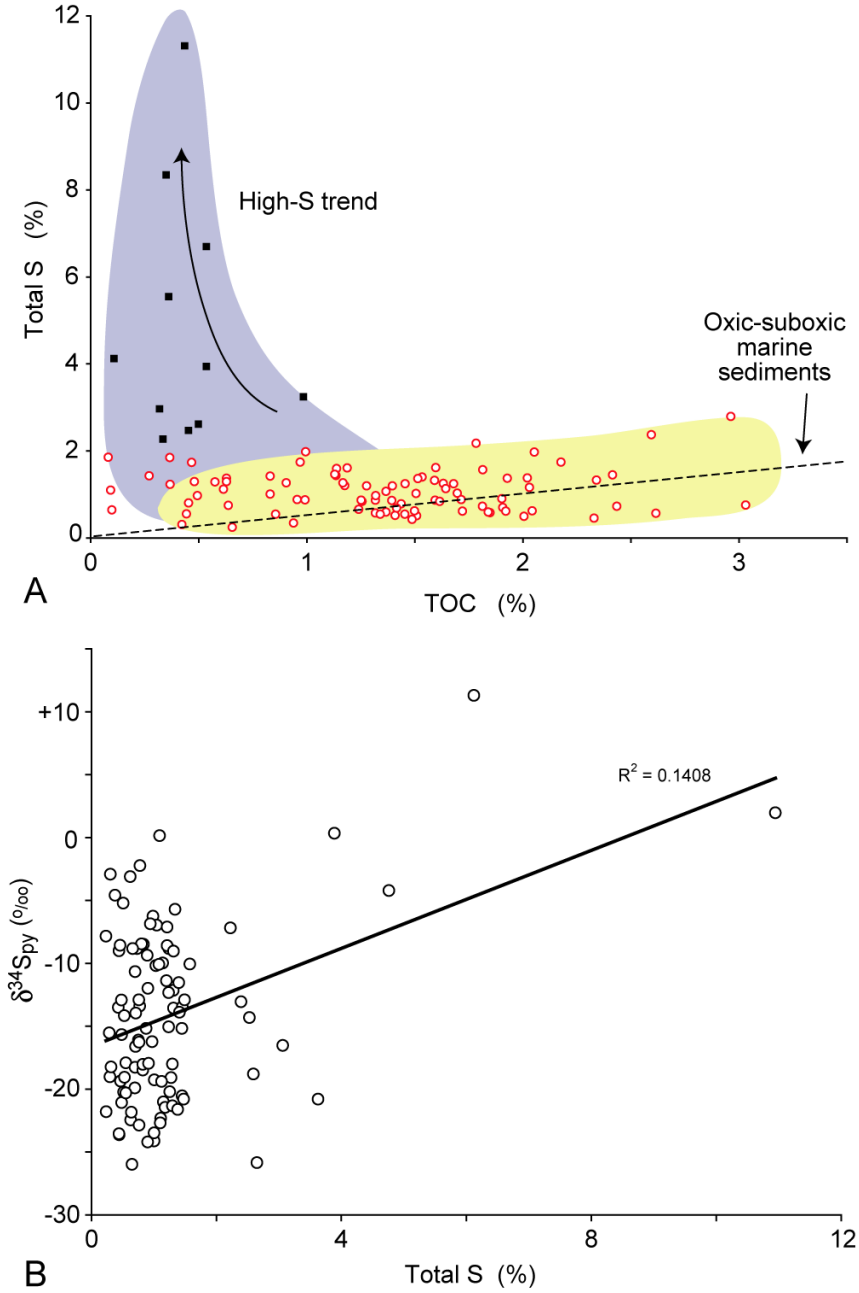
12
10
8
6
4
2
0
Total S (%)
High-S trend
Oxic-suboxic
marine
sediments
0
1
2
3
A
TOC (%)
+10
0
-10
-20
-30
$\delta^{34}S_{py}$ (‰)
R^2 = 0.1408
0
4
8
12
B
Total S (%)

Figure 6.

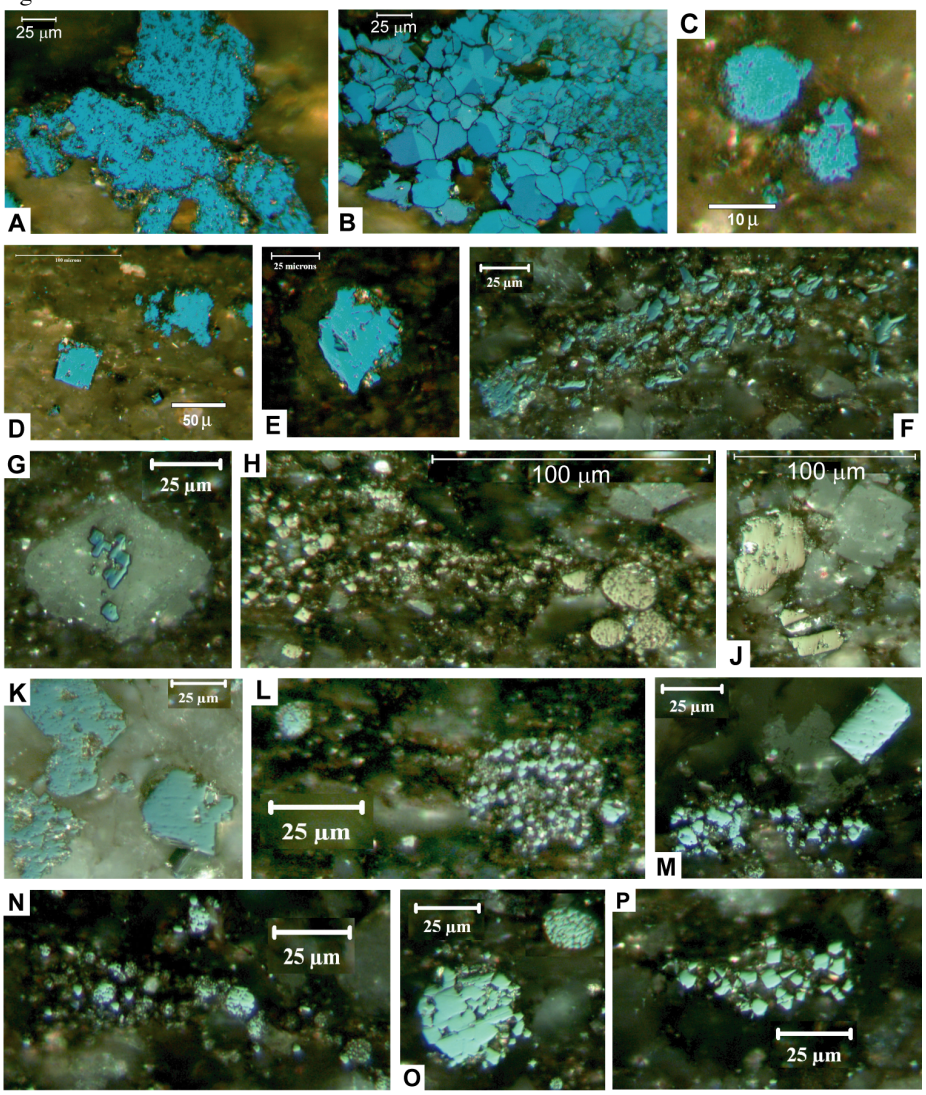
25 µm
A
25 µm
B
C
10 µ
D
50 µ
25 microns
E
25 µm
F
G
25 µm
H
100 µm
100 µm
J
K
25 µm
L
25 µm
25 µm
M
N
25 µm
25 µm
O
P
25 µm

Figure 7.

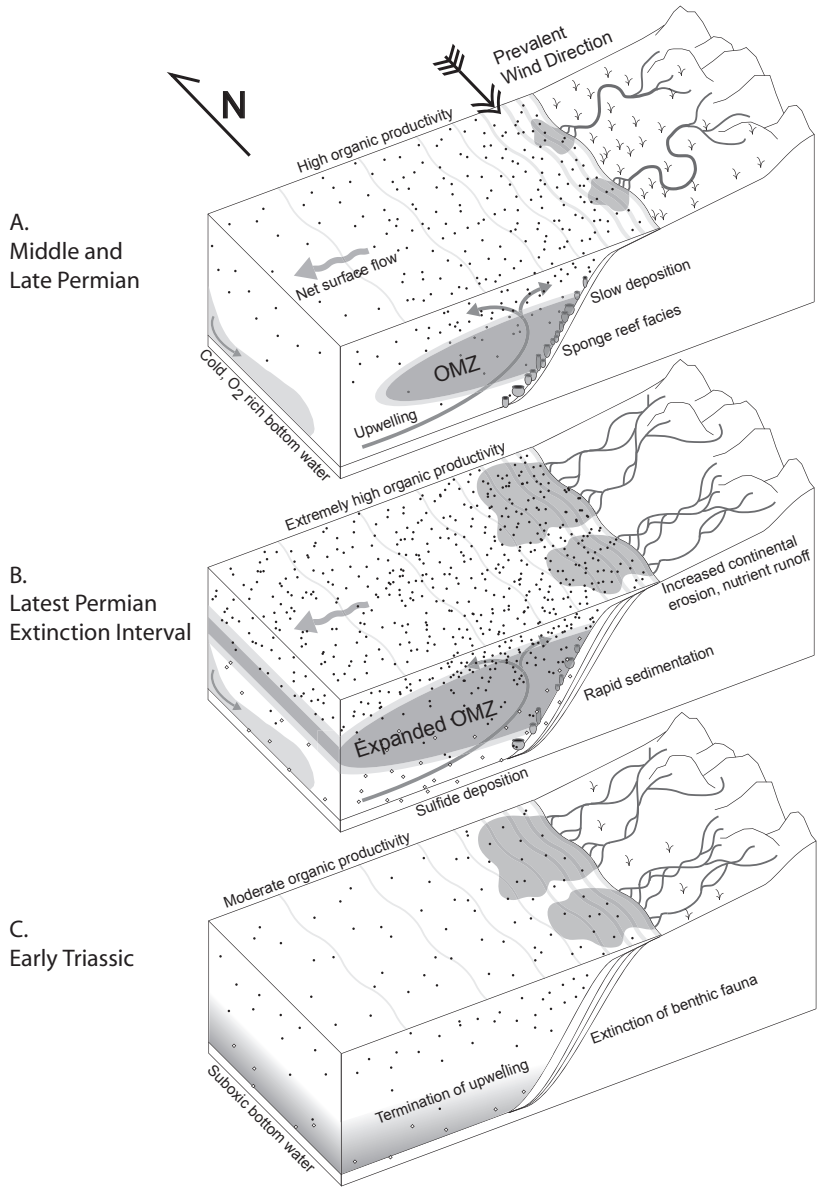
N
Prevalent Wind Direction
A.
Middle and
Late Permian
High organic productivity
Net surface flow
Slow deposition
Sponge reef facies
OMZ
Upwelling
Cold, O2 rich bottom water
B.
Latest Permian
Extinction Interval
Extremely high organic productivity
Increased continental erosion, nutrient runoff
Rapid sedimentation
Expanded OMZ
Sulfide deposition
C.
Early Triassic
Moderate organic productivity
Extinction of benthic fauna
Termination of upwelling
Suboxic bottom water